Scientific Research Publishing

Journal of Power and Energy Engineering, 2019, 7, 71-124
http://www.scirp.org/journal/jpee
ISSN Online: 2327-5901
ISSN Print: 2327-588X

Near-Surface Wind-Speed Stilling in Alaska during 1984-2016 and Its Impact on the Sustainability of Wind Power

Gerhard Kramm[1*], Nicole Mölders[2], John Cooney[3], Ralph Dlugi[4]

[1]Engineering Meteorology Consulting, Fairbanks, AK, USA
[2]Department of Atmospheric Sciences and Geophysical Institute, University of Alaska Fairbanks, Fairbanks, AK, USA
[3]Department of Atmospheric Sciences, Texas A&M University, College Station, TX, USA
[4]Arbeitsgruppe Atmosphärische Prozesse (AGAP), Munich, Germany
Email: *gerhardkramm46@gmail.com

How to cite this paper: Kramm, G., Mölders, N., Cooney, J. and Dlugi, R. (2019) Near-Surface Wind-Speed Stilling in Alaska during 1984-2016 and Its Impact on the Sustainability of Wind Power. *Journal of Power and Energy Engineering*, **7**, 71-124.
https://doi.org/10.4236/jpee.2019.77006

Received: June 13, 2019
Accepted: July 28, 2019
Published: July 31, 2019

Abstract

Based on wind-speed records of Alaska's 19 first-order weather stations, we analyzed the near-surface wind-speed stilling for January 1, 1984 to December 31, 2016. With exception of Big Delta that indicates an increase of 0.0157 $m \cdot s^{-1} \cdot a^{-1}$, on average, all other first-order weather stations show declining trends in the near-surface wind speeds. In most cases, the average trends are less then -0.0300 $m \cdot s^{-1} \cdot a^{-1}$. The strongest average trend of -0.0500 $m \cdot s^{-1} \cdot a^{-1}$ occurred at Homer, followed by -0.0492 $m \cdot s^{-1} \cdot a^{-1}$ at Bettles, and -0.0453 $m \cdot s^{-1} \cdot a^{-1}$ at Yakutat, while the declining trend at Barrow is marginal. The impact of the near-surface wind-speed stilling on the wind-power potential expressed by the wind-power density was predicted and compared with the wind-power classification of the National Renewable Energy Laboratory and the Alaska Energy Authority. This wind-power potential is, however, of subordinate importance because wind turbines only extract a fraction of the kinetic energy from the wind field characterized by the power efficiency. Since wind turbine technology has notably improved during the past 35 years, we hypothetically used seven currently available wind turbines of different rated power and three different shear exponents to assess the wind-power sustainability under changing wind regimes. The shear exponents 1/10, 1/7, and 1/5 served to examine the range of wind power for various conditions of thermal stratification. Based on our analysis for January 1, 1984 to December 31, 2016, Cold Bay, St. Paul Island, Kotzebue, and Bethel would be very good candidates for wind farms. To quantify the impact of a changing wind regime on wind-power sustainability, we predicted wind power for the periods January 1, 1984 to December 31, 1994 and January 1, 2006 to December 31, 2016

as well. Besides Big Delta that suggests an increase in wind power of up to 12% for 1/7, predicted wind power decreased at all sites with the highest decline at Annette (≈38%), Kodiak (≈30%), King Salmon (≈26%), and Kotzebue (≈24%), where the effect of the shear exponents was marginal. Bethel (up to 20%) and Cold Bay (up to 14%) also show remarkable decreases in predicted wind power.

Keywords

Near-Surface Wind Speed, Wind Power, Wind-Power Potential, Wind-Power Density, Wind-Speed Stilling, Energy Flux Budget, Sensible and Latent Heat

1. Introduction

There is observational evidence of declining trends in the near-surface wind speeds over the last five decades in numerous areas of the world [1]. Decreases in wind speeds have occurred, for instance, in Australia [2] [3], United States [4] [5] [6], China [7] [8] [9], Italy [10], Canada [11] [12], Spain and Portugal [13] [14], Alaska [15] [16], Canary Islands [17], and other locations in Europe and Asia [6]. Roderick *et al.* [3] already termed these declining trends as "stilling".

McVicar *et al.* [1] analyzed 148 studies reporting terrestrial trends of the wind speed at anemometer height, $v_R = |\boldsymbol{v}_R|$, from across the globe (with uneven and incomplete spatial distribution and differing periods of measurement). They found an average trend of -0.014 m·s^{-1}·a^{-1} for studies with more than 30 sites with observing data for more than 30 years. Assuming, for instance, a linear trend, these declining trends constitute a -0.70 m·s^{-1} change in v_R over 50 years [1]. Their review (a) gives evidence that terrestrial stilling is widespread across the globe; (b) confirms declining rates of evaporative demand, and (c) highlights the contribution v_R has made to these declining evaporative rates. The terrestrial stilling has been attributed to various causes (e.g., [1] [13] [14], and the relevant references therein). The exact causes, however, have not yet been identified [17].

Terrestrial stilling is, however, not omnipresent. Some positive trends were reported by McVicar *et al.* [1]. The situation is rather complex as indicated by the observations performed at the first-order weather station Barrow (now the City of Utqiaġvik), Alaska (for the specification, see **Table 1**). Based on the period 1921-2001, Lynch *et al.* [18] found a positive trend of 0.0047 m·s^{-1}·a^{-1}. In addition, Hartmann and Wendler [16] found an increase in wind speed of 0.4 m·s^{-1}·a^{-1} when comparing period 1951 - 1975 with that of 1977 - 2001 related by these authors to the 1976 Pacific climate shift when the Pacific Decadal Oscillation index changed from the mainly negative values during the first 25-year period to the mainly positive values during the second one. On the contrary, we found a marginal decrease for the period January 1, 1984 to December 31, 2016 denoted as Period I hereafter. Nonetheless, the worldwide evidence for declining

near-surface wind speeds and their impact on the sustainability of wind power demands care and attention.

The objective of our paper is two-fold: (a) to provide additional evidence to the process of near-surface wind-speed stilling in Alaska during Period I, and (b) to quantify the impact of a changing wind regime on the wind-power sustainability in the statewide region by considering the change from the period January 1, 1984 to December 31, 1994 denoted as Period II hereafter to the period January 1, 2006 to December 31, 2016 denoted as Period III hereafter. This means that the Period I was divided into three equal periods of 11 years.

To achieve these goals, we consider Alaska's 19 first-order weather stations as a testbed. First-order stations are defined as those operated by certified observers and are typically operated by the National Weather Service. These sites include a full suite of equipment to measure air pressure and temperature, cloudiness, total precipitation, snowfall, wind speed and wind direction (e.g. [16]). These stations are grouped into climate regions and their specifications are listed in **Table 1**.

Declining trends in the near-surface wind speeds notably affect the wind-power potential [6] commonly expressed by the wind-power density (*i.e.*, the mean kinetic energy stream density) at a certain height above the surface [19],

$$\overline{\boldsymbol{S}_{kin}} = \frac{\overline{\rho}}{2}\left(\hat{\boldsymbol{v}}^2 + \widehat{\boldsymbol{v}''^2}\right)\hat{\boldsymbol{v}} + \frac{1}{2}\overline{\rho \boldsymbol{v}'' \boldsymbol{v}''^2}, \tag{1.1}$$

This equation describes the transfer of mean kinetic energy (MKE) and turbulent kinetic energy (TKE) by the mean wind field and the transfer of TKE by the eddying wind field. Here, ρ and $\boldsymbol{v}$ are the air density and the velocity of the wind field at the same height, respectively. The overbar $(\overline{\ldots})$ characterizes the conventional Reynolds mean and a prime $(')$ the deviation from that. The hat $(\widehat{\ldots})$ denotes the density-weighted average according to Hesselberg [20] defined by

$$\hat{\chi} = \frac{\overline{\rho\chi}}{\overline{\rho}}, \tag{1.2}$$

and the double prime $('')$ marks the departure from that. Here, χ is a field quantity like the wind vector, $\boldsymbol{v}$, and the specific humidity m_1. It is obvious that $\overline{\rho\chi''} = \overline{\rho\chi''} = 0$. Hesselberg's average can be related to that of Reynolds by [21] [22] [23] [24] [25].

$$\hat{\chi} = \overline{\chi} + \frac{\overline{\rho'\chi'}}{\overline{\rho}} = \overline{\chi}\left\{1 + \frac{\overline{\rho'\chi'}}{\overline{\rho}\,\overline{\chi}}\right\}. \tag{1.3}$$

Obviously the different means $\hat{\chi}$ and $\overline{\chi}$, are nearly equal if $\left|\overline{\rho'\chi'}\middle/\left\{\overline{\rho}\,\overline{\chi}\right\}\right| \ll 1$ as used, for instance, in case of the Boussinesq approximation. The Hesselberg average of the wind vector, for instance, is given by $\hat{\boldsymbol{v}} = \overline{\rho\boldsymbol{v}}/\overline{\rho}$. Note that intensive quantities like air pressure, p_a, and air density, ρ, are averaged in the sense of Reynolds. Arithmetic rules are given by [21] [23] [26] [27]. Hesselberg's

Table 1. Specifications of the first-order stations of the National Weather Service in Alaska, USA, where z_R is the anemometer height.

Station and ID Numbers		Location	Latitude	Longitude	Elevation (m)	z_R (m)
1	USW00027502	Barrow WSO	71.2883˚N	156.7814˚W	9.4	8
2	USW00026533	Bettles	66.9161˚N	151.5089˚W	195.7	10
3	USW00026411	Fairbanks INTL	64.8039˚N	147.8761˚W	131.7	10
4	USW00026415	Big Delta FAA/AMOS	63.9944˚N	145.7214˚W	389.2	10
5	USW00026510	McGrath	62.9575˚N	155.6103˚W	101.5	10
6	USW00026425	Gulkana	62.1592˚N	145.4589˚W	476.1	10
7	USW00026616	Kotzebue WSO	66.8667˚N	162.6333˚W	9.1	8
8	USW00026617	Nome WSO	64.5111˚N	165.4400˚W	4	8
9	USW00026615	Bethel	60.7850˚N	161.8292˚W	31.1	8
10	USW00026528	Talkeetna	62.3200˚N	150.0950˚W	106.7	8
11	USW00026451	Anchorage INTL	61.1689˚N	150.0278˚W	36.6	8
12	USW00025507	Homer	59.6419˚N	151.4908˚W	19.5	8
13	USW00025503	King Salmon	58.6794˚N	156.6294˚W	19.2	10
14	USW00025339	Yakutat	59.5119˚N	139.6711˚W	10.1	10
15	USW00025309	Juneau	58.3567˚N	134.5639˚W	4.9	10
16	USW00025308	Annette WSO	55.0389˚N	131.5786˚W	33.2	10
17	USW00025713	St. Paul Island	57.1553˚N	170.2222˚W	10.7	10
18	USW00025501	Kodiak	57.7511˚N	152.4856˚W	24.4	10
19	USW00025624	Cold Bay	55.2208˚N	162.7325˚W	23.8	10

density-weighted averaging procedure is well appropriate to formulate the balance equation for turbulent systems [19] [21] [23] [24] [26]-[33].

Ignoring in Equation (1.1) the turbulent effects yields

$$\overline{\boldsymbol{S}_{kin}} = \frac{1}{2}\overline{\rho \hat{\boldsymbol{v}}^2 \hat{\boldsymbol{v}}}. \tag{1.4}$$

The magnitude of $\overline{\boldsymbol{S}_{kin}}$ is given by

$$S_{kin} = \left|\overline{\boldsymbol{S}_{kin}}\right| = \frac{1}{2}\overline{\rho \hat{\boldsymbol{v}}^2}\left|\hat{\boldsymbol{v}}\right| = \frac{1}{2}\overline{\rho \hat{v}^3}, \tag{1.5}$$

where $\hat{v} = \left|\hat{\boldsymbol{v}}\right|$. Apparently, the wind-power density is proportional to the cube of wind speed. The rotor of a wind turbine causes a divergence effect expressed by $\nabla \cdot \overline{\boldsymbol{S}_{kin}} \neq 0$. The wind speed is usually assumed as uniformly distributed over the rotor area of a wind turbine which is a crude assumption. Generally, at a given location, all these quantities vary with time.

As wind turbines only extract a fraction of the kinetic energy from the wind field characterized by the power efficiency (see, e.g., [19] [34] and **Figure 1**),

$$C_P = \frac{P}{P_\infty}, \tag{1.6}$$

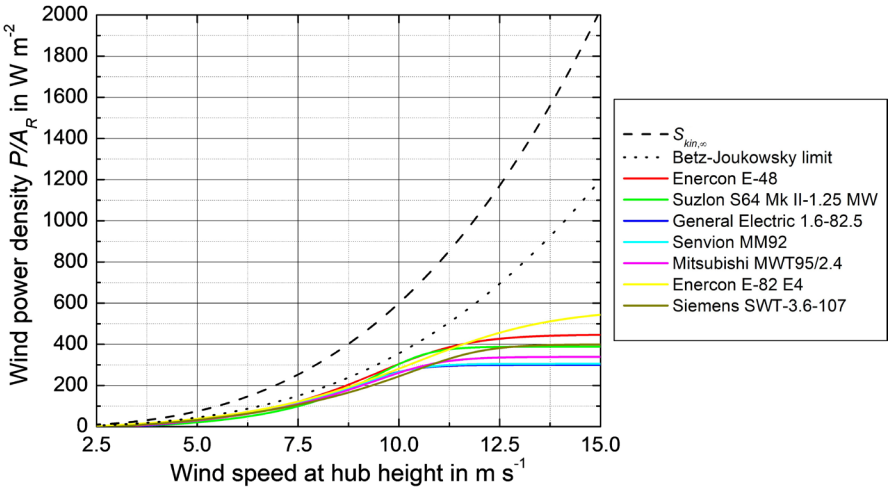

Figure 1. Wind-power densities of the seven wind turbines listed in **Table 2**. Also shown are the wind-power density $S_{kin,\infty}$ given by Equation (1.5), and $S_{kin,\infty}$ weighted by the Betz-Joukowsky limit $C_P = 16/27 \cong 0.593$ (adopted from [19]).

the wind-power potential is of subordinate importance. Here, P is the extracted (or consumed) power, and

$$P_\infty = \frac{1}{2}\overline{\rho A_R \widehat{v_\infty}^3} = A_R S_{kin,\infty}, \tag{1.7}$$

is the power carried by the flow through the projection of the turbine section region onto the plane perpendicular to it, where v_∞ is the undisturbed wind speed far upstream of the wind turbine, and A_R is the rotor area considered as perpendicular to the flow axis.

Therefore, it is indispensable to analyze how wind turbines respond to the declining trends in near-surface wind speeds. Since the wind turbine technology has notably improved during the past 35 years, we followed Mölders *et al.* [15] and used seven currently available wind turbines of different rated power to assess the wind-power sustainability under changing wind regimes. These wind turbines are: Enercon E-48, Suzlon S64 Mark II-1.25 MW, General Electric 1.6 - 82.5, Senvion MM92 (formerly known as RE Power MM92), Mitsubishi MWT95/2.4, Enercon E-82 E4, and Siemens SWT-3.6-107. They were chosen because their rated power increases by an increment of about 400 kW. Some of their technical specifications are listed in **Table 2.** Senvion MM92 and Mitsubishi MWT95/2.4 were also used by Mölders *et al.* [35] in their study on the uncertainty in wind-power assessment over complex terrain.

In Section 2, we describe the data source and the methodology. Here, we also compare the wind-power potential obtained from daily mean averages of wind speed with that based on hourly mean averages of wind speed for the same time interval because the latter is generally larger than the former. This comparison serves for assessing the results of our wind-power predictions for the Periods I, II, and III that are based on daily mean averages of wind speed taken from the Global Historical Climatology Network (GHCN)-Daily [36]. The impact of the

Table 2. Specifications of the wind turbines considered in this study (adopted from Kramm *et al.* [19]).

Wind turbine	Hub height (m)	Swept area (m^2)	Cut-in wind speed ($m \cdot s^{-1}$)	Rated wind speed ($m \cdot s^{-1}$)	Cut-out wind Speed ($m \cdot s^{-1}$)	Rated power (kW)	Wind Class
Enercon E-48	76	1810	2-3	13.5	25	800	IEC IIa
Suzlon S64 Mark II-1.25 MW	74.5	3217	4	12.0	25	1250	IIa
General Electric 1.6-82.5	80	5345	3.5	11.5	25	1600	IEC IIIb
Senvion MM92	78-80	6720	3	12.5	24	2050	IEC IIa
Mitsubishi MWT95/2.4	80	7088	3	12.5	25	2400	IEC IIa
Enercon E-82 E4	78/84	5281	2-3	16	25	3000	IEC IIa
Siemens SWT-3.6-107	80	9000	3	14.0	25	3600	IEC Ia

near-surface wind-speed stilling on the energy conversion at the interface Earth-atmosphere and the wind power is analyzed in Section 3. Note that the decreasing evapotranspiration as reported by McVicar *et al.* [1] also affects the energy conversion at the interface Earth-atmosphere. Our method to predict the wind power using the seven currently available wind turbines of different rated power listed in **Table 2** is outlined in Section 4. The results are presented in Section 5.

2. Wind Data and Methodology

To estimate the wind-power potential in Alaska, we considered the daily mean wind data provided by the 19 first-order weather stations in Alaska for Periods I, II, and III. The wind data are taken from the Global Historical Climatology Network (GHCN)-Daily [36]. Days for which no wind data were reported were removed from the datasets. The number of days considered is listed in **Table 3**. Anemometer heights were taken from http://www.nws.noaa.gov/ops2/Surface/documents/windtower.xls.

Based on these wind data, we assessed these locations for their suitability for wind farms by answering three major questions:

1) Does the location exhibit enough wind speed to generate electrical power in a sufficient manner?

2) Is this electrical power affected by long-term trends in horizontal wind speeds?

3) Are there obstacles such as siting issues present at the location?

The first two questions relate to the basic requirements for establishing a wind farm. The third question assesses the impacts of any kind of energy producing facilities (e.g., power plants fueled with coal, oil, gas, or nuclear elements to hydroelectric dams, tide-power systems, wind farms) on the natural environment. The impact of wind farms on endangered species, avian migrations/habitats, wetlands/protected areas, and subsistence lifestyle must be considered as well. Additionally, for numerous Alaska areas, the ambient temperatures fall below −20˚C in winter which is below the operation range of most wind turbines, except cold climate versions like that of Senvion MM92 which has a lower limit of −30˚C. Frequently icing of rotor blades due to the occurrence of supercooled

water in the lower atmospheric boundary layer may affect the outcome of wind power as well. The answers to these questions served as the foundation for evaluating each site in terms of cost-benefits analyses.

First, we analyzed whether the wind speeds observed at a given location during the period under study satisfy the minimum average wind speed requirement. A site must have a minimum annual average wind speed of, at least 4.9 $\mathrm{m\cdot s^{-1}}$ to 5.8 $\mathrm{m\cdot s^{-1}}$ to be considered (American Wind Energy Association, 2009).

The average $\langle v_R \rangle$ for each station was calculated using

$$\langle v_R \rangle = \frac{1}{T_N}\int_{T_0}^{T_N} v_R(t)\,\mathrm{d}t = \frac{T_d}{T_N}\left(\frac{1}{T_d}\int_{T_0}^{T_1} v_{R,1}(t)\,\mathrm{d}t + \frac{1}{T_d}\int_{T_1}^{T_2} v_{R,2}(t)\,\mathrm{d}t + \cdots + \frac{1}{T_d}\int_{T_{N-1}}^{T_N} v_{R,N}(t)\,\mathrm{d}t\right), \tag{2.1}$$

where t is time, $T_N = NT_d$ is the period under study, N is the number of days, $T_d = T_i - T_{i-1}$, $i = 1,2,\cdots,N$, is the time period of a day, and $v_R(t) = |\boldsymbol{v}_R(t)|$ is the time-dependent horizontal wind speed at anemometer height that usually amounts to $z_R \cong 10\ \mathrm{m}\,(\cong 33\ \mathrm{ft})$ above the surface. At seven of the 19 first-order stations, wind speed is measured at a height of $z_R \cong 8\ \mathrm{m}\,(\cong 26\ \mathrm{ft})$. For all first-order stations, linear trends in daily mean wind speeds are listed in **Table 3** for Period I.

Equation (2.1) provides the average wind speed for each station. Introducing the daily mean wind speed by

$$\overline{v_{R,i}} = \frac{1}{T_d}\int_{T_{i-1}}^{T_i} v_{R,i}(t)\,\mathrm{d}t, \tag{2.2}$$

where $v_{R,i}(t)$ is the wind speed at anemometer height for the time $[T_{i-1}, T_i]$ of the i^{th} day, leads to

$$\langle v_R \rangle = \frac{1}{N}\sum_{i=1}^{N}\overline{v_{R,i}}. \tag{2.3}$$

As described in the Wind Energy Resource Atlas of the United States, another measure for assessing the wind-power potential at a given location is related to the wind-power class listed in **Figure 2**. It is based on the true wind-power density at the height of $z = 50\ \mathrm{m}$ above ground. The average of the wind-power density is given by

$$\langle S_{kin,z} \rangle = \frac{1}{2T_N}\int_{0}^{T_N} \rho_z(t) v_z^3(t)\,\mathrm{d}t. \tag{2.4}$$

Here, $\rho_z(t)$ is the air density, and $v_z(t)$ is the wind speed at z. Similar to Equation (2.1), we obtain

$$\langle S_{kin,z} \rangle = \frac{T_d}{2T_N}\left(\frac{1}{T_d}\int_{T_0}^{T_1} \rho_{z,1}(t) v_{z,1}^3(t)\,\mathrm{d}t + \frac{1}{T_d}\int_{T_1}^{T_2} \rho_{z,2}(t) v_{z,2}^3(t)\,\mathrm{d}t + \cdots + \frac{1}{T_d}\int_{T_{N-1}}^{T_N} \rho_{z,N}(t) v_{z,N}^3(t)\,\mathrm{d}t\right) \tag{2.5}$$

where $\rho_{z,i}(t)$ and $v_{z,i}^3(t)$ are related to the time of the i^{th} day.

Table 3. Average wind speed, $\langle v_R \rangle$, and change in wind speed expressed (a) by a linear trend, $\Delta v_{R,a}$, and (b) by the Period I-averaged change, $\Delta v_{R,PI}$ at first-order stations of the National Weather Service in Alaska, USA, where N is the number of days used in our analysis.

Location	N	$\langle v_R \rangle$ m·s^{-1}	$\Delta v_{R,a}$ m·s^{-1}·a^{-1}	$\Delta v_{R,PI}$ m·s^{-1}
Barrow WSO	12,011	5.63	−0.0001	−0.03
Bettles	11,629	2.43	−0.0492	−1.62
Fairbanks INTL	12,019	1.97	−0.0368	−1.21
Big Delta FAA/AMOS	11,333	4.13	0.0157	0.52
McGrath	12,031	2.00	−0.0405	−1.33
Gulkana	11,552	2.51	−0.0043	−0.14
Kotzebue WSO	12,023	5.24	−0.0395	−1.30
Nome WSO	11,991	4.18	−0.0221	−0.73
Bethel	12,052	5.22	−0.0269	−0.89
Talkeetna	11,914	2.01	−0.0389	−1.28
Anchorage INTL	12,052	3.10	−0.0310	−1.02
Homer	12,033	3.14	−0.0500	−1.65
King Salmon	12,054	4.33	−0.0313	−1.03
Yakutat	12,039	2.52	−0.0453	−1.50
Juneau	11,556	3.33	−0.0205	−0.68
Annette WSO	12,047	3.56	−0.0426	−1.40
St. Paul Island	11,990	6.92	−0.0173	−0.57
Kodiak	12,049	4.84	−0.0450	−1.48
Cold Bay	12,051	7.19	−0.0391	−1.29

Introducing the respective daily mean value of this true wind-power density by

$$\overline{S_{kin,z,i}} = \frac{1}{2T_d} \int_{T_{i-1}}^{T_i} \rho_{z,i}(t) v_{z,i}^3(t) \mathrm{d}t \tag{2.6}$$

provides

$$\langle s_{kin,z} \rangle = \frac{1}{N} \sum_{i=1}^{N} \overline{S_{kin,z,i}} \,. \tag{2.7}$$

Unfortunately, the wind speed data taken from the GHCN-Daily do not allow to precisely compute $\overline{S_{kin,z,i}}$. Even if we consider air density as nearly constant for the i^{th} day (which leads to the so-called anelastic approximation of the equation of continuity), we have to acknowledge that

$$\left(\overline{v_{z,i}}\right)^3 \le \overline{v_{z,i}^3} \,. \tag{2.8}$$

This inequality can be verified using Hölder's inequality for integrals,

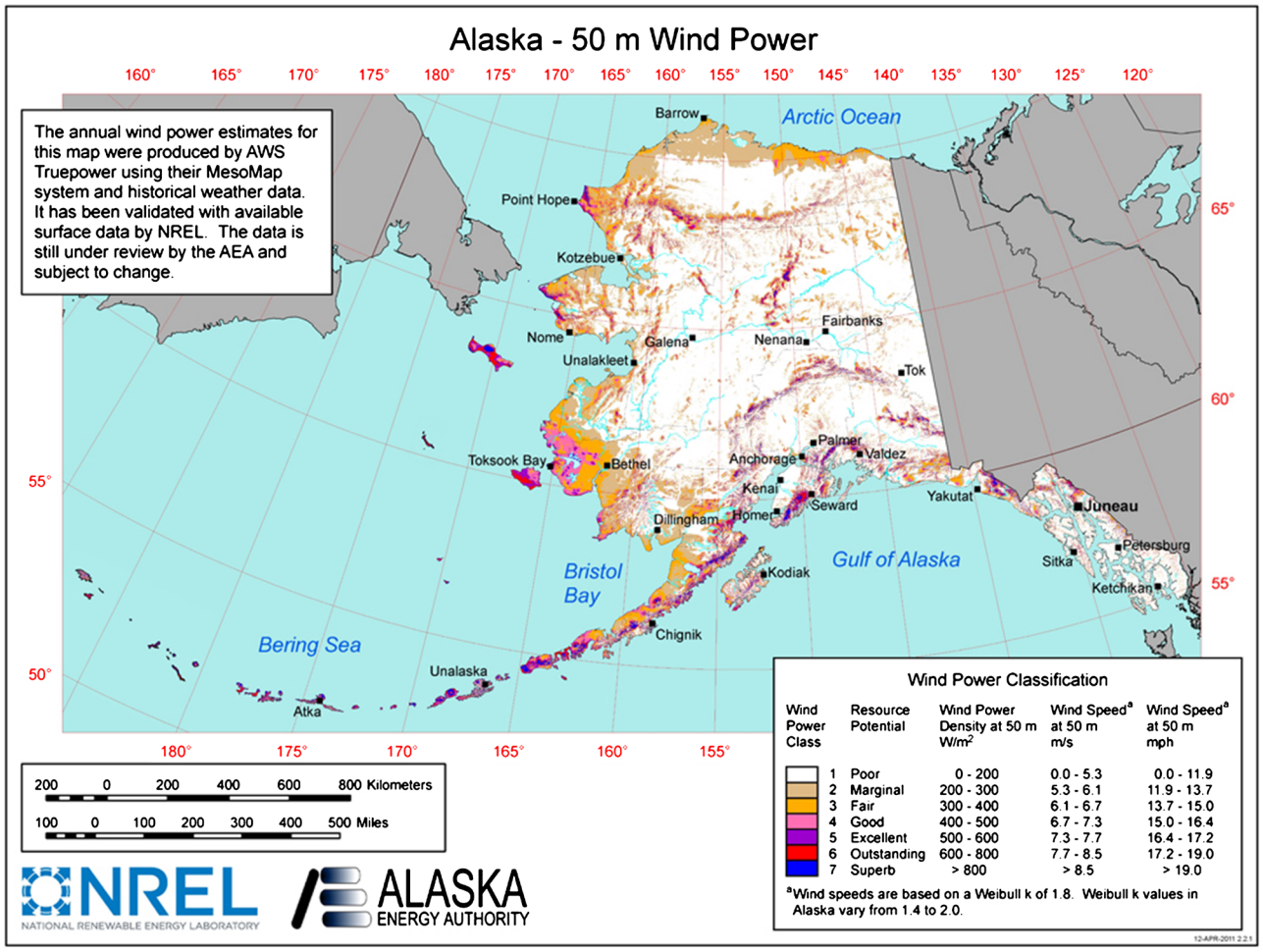

Figure 2. Wind-power classification according to National Renewable Energy Laboratory and the Alaska Energy Authority.

$$\left|\int_a^b f(x)g(x)\,\mathrm{d}x\right| \le \left(\int_a^b |f(x)|^{p_h}\,\mathrm{d}x\right)^{\frac{1}{p_h}} \left(\int_a^b |g(x)|^{q_h}\,\mathrm{d}x\right)^{\frac{1}{q_h}}, \tag{2.9}$$

where $p_h \in (1,\infty)$ and q_h are conjugate exponents obeying

$$\frac{1}{p_h}+\frac{1}{q_h}=1, \tag{2.10}$$

i.e., $q_h = p_h/(p_h-1)$. Furthermore, $f(x)$ and $g(x)$ are real functions ($f,g:[a,b]\to\mathbb{R}$). For the two non-negative measurable functions $f(x)=v_{z,i}(x)$ and $g(x)=1$ as well as $p_h=3 \Rightarrow q_h=3/2$, and $x=t/T_d$, we obtain

$$\overline{v_{z,i}} = \int_0^1 v_{z,i}(x)\,\mathrm{d}x \le \left(\int_0^1 v_{z,i}^3(x)\,\mathrm{d}x\right)^{\frac{1}{3}} = \left(\overline{v_{z,i}^3}\right)^{\frac{1}{3}} \tag{2.11}$$

and in a further step the Inequality (2.8). Differences

$$\Delta v^3 = \frac{\overline{v_{z,i}^3}-\left(\overline{v_{z,i}}\right)^3}{\overline{v_{z,i}^3}} \tag{2.12}$$

are illustrated in **Figure 3** and **Figure 4** for two different cases. **Figure 3** is based

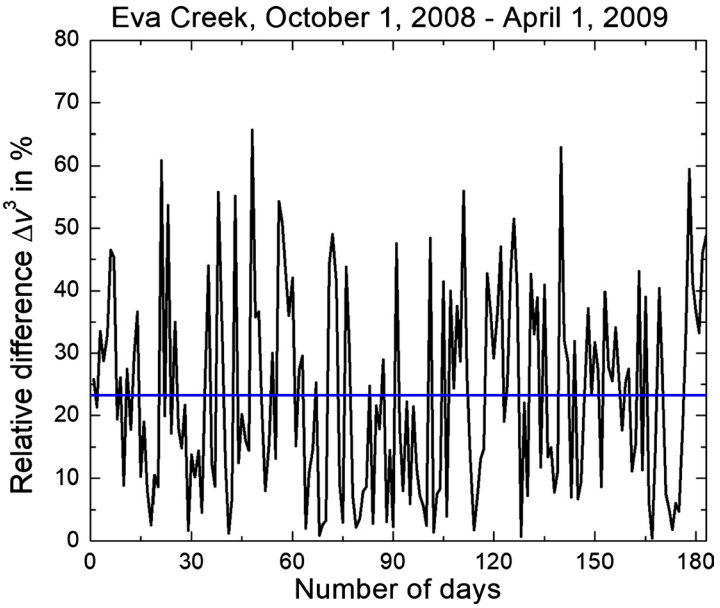

Figure 3. Time series of the relative difference Δv^3 in wind-power density (given by Equation (2.12)) representative for the height interval from 64 m to 113 m above ground level (black line). The hourly wind speed data stem from WRF/chem model simulations performed for the area of the Eva Creek wind farm in Interior Alaska for October 1, 2008 to April 1, 2009 ([38] [34]). The blue line indicates the mean value of $\Delta v^3 = 23.3\%$.

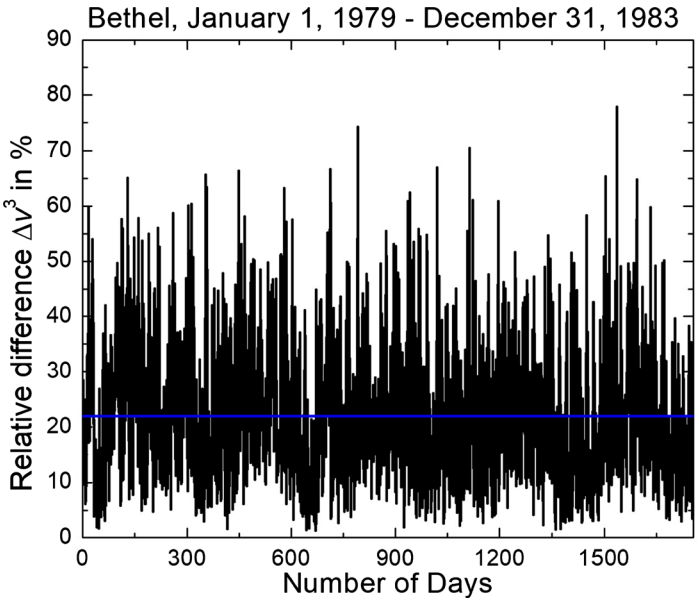

Figure 4. As in **Figure 3**, but the hourly mean wind speeds are related to the measurements performed at first-order weather station Bethel (anemometer height of $z_R = 8\ \mathrm{m}(26\ \mathrm{ft})$). The corresponding daily mean wind speeds illustrated in **Figure 5** covered the period from January 1, 1979 to December 31, 1983. The blue line indicates the mean value of $\Delta v^3 = 21.9\%$.

on WRF/chem model simulations performed for the area of the Eva Creek wind farm in Interior Alaska. This mean wind speed is representative for heights between 64 and 113 m above ground level [34] [37]. Daily mean wind speeds were

computed using hourly mean wind speeds. The figure shows that the Inequality (2.8) is always fulfilled.

Figure 4 is based on the hourly mean wind speeds related to observations at Bethel (anemometer height of $z_R = 8\,\mathrm{m}(26\,\mathrm{ft})$) from January 1, 1979 to December 31, 1983. Missing data were replaced by interpolated values to obtain an adequate dataset of daily mean wind speeds (**Figure 5**). Nevertheless, 70 of these daily mean wind speeds were removed from the dataset because of too many missing hourly mean wind speeds. Apparently, these daily mean wind speeds decreased. Again, the Inequality (2.8) is always fulfilled. Since the wind-power potential is of subordinate importance, we analyze how the chosen wind turbines (see **Table 2**) respond to this difference in the wind-power potential (see Section 5).

The daily mean wind speed, $\overline{v_{R,i}}$, is based on observations performed at anemometer height z_R. To compute the mean wind speed at higher levels than the anemometer height, $z > z_R$, commonly the power-law profile (e.g., [38] [39] [40] [41] [42]),

$$\overline{v_{z,i}} = \overline{v_{R,i}}\left(\frac{z}{z_R}\right)^{p_i}, \tag{2.13}$$

is used, where $v_{z,i}$ and $v_{R,i}$ are the wind speeds at the heights z and z_R, respectively. Here, the shear exponent ranges from $p_i = 1/7$ for near-neutral stability conditions to $p_i = 1/10$ for strong lapse rates. Frost [43] reported that for extremely stable stratification, $p_i = 8/10$ may be possible. Generally, p_i varies in the diurnal course and depends on the surface roughness and the height of the level under evaluation (e.g., [40] [41] [43] [44] [45] [46]). Based on the study

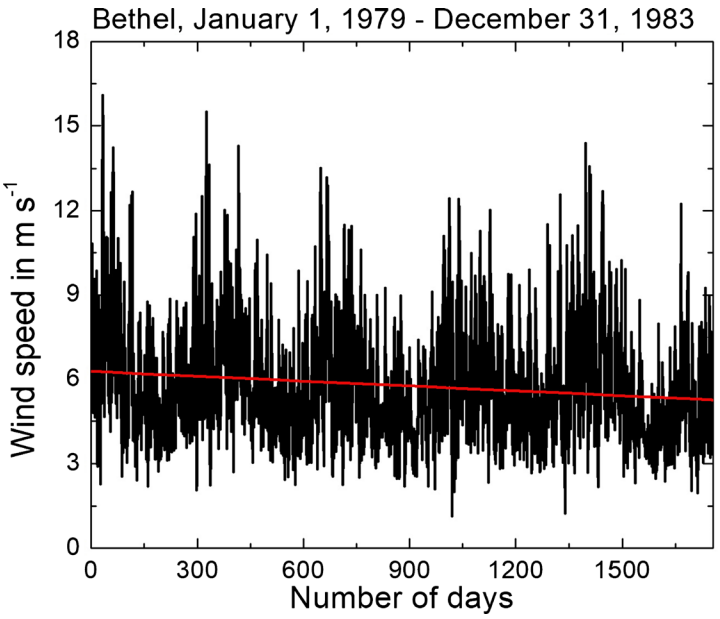

Figure 5. Daily mean wind speeds (black line) related to the measurements at the anemometer height of $z_R = 8\,\mathrm{m}(26\,\mathrm{ft})$ at Bethel for January 1, 1979 to December 31, 1983. The red line illustrates the linear trend. Daily mean wind speeds were computed from hourly mean wind speeds.

of Schwartz and Elliot regarding the wind shear characteristics at Central Plains (Texas to North Dakota) tall towers [40], we used $p_i = 1/5$ as an upper limit.

Since $\overline{v_{R,i}}$ for the i^{th} day is given by

$$\begin{aligned}\overline{v_{R,i}} &= \frac{1}{T_d}\int_0^{T_d} v_{R,i}(t)\,\mathrm{d}t \\ &= \frac{\Delta T}{T_d}\left(\frac{1}{\Delta T}\int_{T_0}^{T_1} v_{R,i}(t)\,\mathrm{d}t + \frac{1}{\Delta T}\int_{T_1}^{T_2} v_{R,i}(t)\,\mathrm{d}t + \cdots + \frac{1}{\Delta T}\int_{T_{M-1}}^{T_M} v_{R,i}(t)\,\mathrm{d}t\right)\end{aligned} \tag{2.14}$$

where $\Delta T = T_k - T_{k-1}$, $k = 1,2,\cdots,M$, $T_0 = 0$, and $T_d = M\Delta T$, M is the number of averaging intervals, for instance, of $\Delta T = 30$ min or $\Delta T = 60$ min. The mean wind speed for the k^{th} averaging interval is then given by

$$\overline{v_{R,i,k}} = \frac{1}{\Delta T}\int_{T_{k-1}}^{T_k} v_{R,i,k}(t)\,\mathrm{d}t\,. \tag{2.15}$$

Thus, we obtain

$$\overline{v_{R,i}} = \frac{1}{M}\sum_{k=1}^{M}\overline{v_{R,i,k}}\,. \tag{2.16}$$

In accord with Equation (2.13), the corresponding wind speed at z amounts to

$$\overline{v_{z,i}} = \frac{1}{M}\sum_{k=1}^{M}\overline{v_{z,i,k}} = \frac{1}{M}\sum_{k=1}^{M}\overline{v_{R,i,k}}\left(\frac{z}{z_R}\right)^{p_{i,k}}\,. \tag{2.17}$$

In case of an exponent $p_{i,k}$ that does not vary with time during the i^{th} day, *i.e.*, $p_{i,k} = p_i$, one obtains Equation (2.13). This equation was used to extrapolate the daily mean wind speeds at z_R to both the level of $z = 50$ m to compute the wind-power density, $\langle S_{kin,z}\rangle$, of the wind field as express by Equation (2.4) and of $z = 80$ m chosen as the hub height of the wind turbines considered in this study. For each first-order weather station, we considered $p = p_i = 1/10$, $p = p_i = 1/7$, and $p = p_i = 1/5$ to cover the range of wind power for various conditions of thermal stratification. Based on these shear exponents, vertical wind profiles were drawn, where $p = p_i = 1/10$ causes the weakest and $p = p_i = 1/5$ produces the strongest increase of wind speed with height (**Figure 6**). Thus, the assumption that the wind speed is uniformly distributed over the rotor area of a wind turbine is rather crude. In situations with strong wind shear, the turbine blades, shaft and roller bearing of the rotor may notably be affected by varying thrust forces during each rotation. Thus, high values of p imply that wind turbines can generate a substantial amount of energy, even when the wind speed near the ground is minimal. Concurrently, larger values of p will introduce higher fatigue loads on the turbine blades [41] [42] [47] [48].

Figure 7 shows the average wind speed determined for each first-order weather station,

$$\langle v_z\rangle = \frac{1}{N}\sum_{i=1}^{N}\overline{v_{z,i}}\,. \tag{2.18}$$

at both $z = 50$ m and $z = 80$ m.

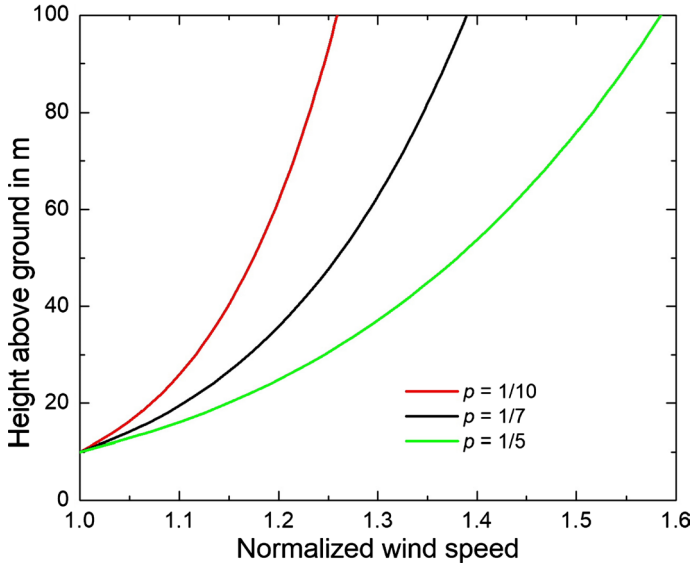

Figure 6. Vertical profiles of the normalized wind speed $\overline{v_{z,i}}/\overline{v_{R,i}}$ (see Equation (2.13)) for the three different shear exponents $p = p_i = 1/10$, $p = p_i = 1/7$, and $p = p_i = 1/5$ used in this study to determine the range of wind power for various conditions of thermal stratification.

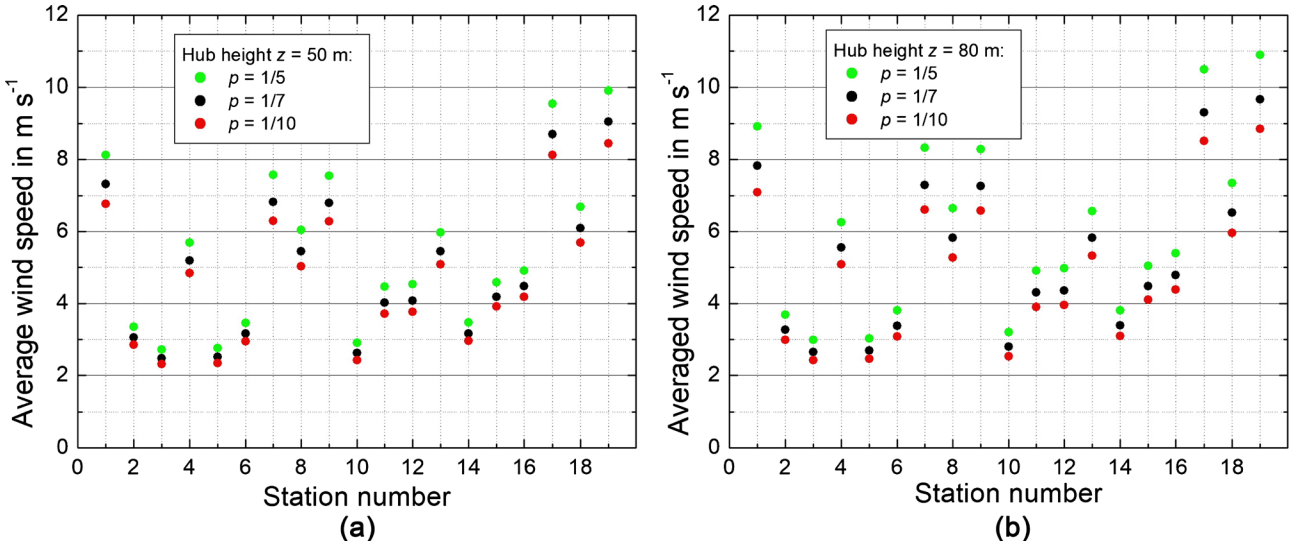

Figure 7. Average wind speed $\langle v_z \rangle$ at Alaska's first-order weather stations computed for both (a) $z = 50$ m and (b) $z = 80$ m above ground level, respectively (see **Table 1** for station numbers).

The respective mean wind-power density $\langle S_{kin,z} \rangle$ (see Equation (2.4)) at these heights is illustrated in **Figure 8**. According to these figures and the wind-power classification listed in **Figure 2**, we do not further consider sites that are related to a wind-power class of 1 (termed as "poor") like Bettles (2), Fairbanks (3), McGrath (5), Gulkana (6), Talkeetna (10), Anchorage (11), Homer (12), and Yakutat (14) in our wind-power analysis, despite their declining trends in the near-surface wind speed. These stations would be impractical options for wind farms because they were unable to meet the basic criteria. The wind speeds at these locations would not be high enough to sufficiently supply power to the

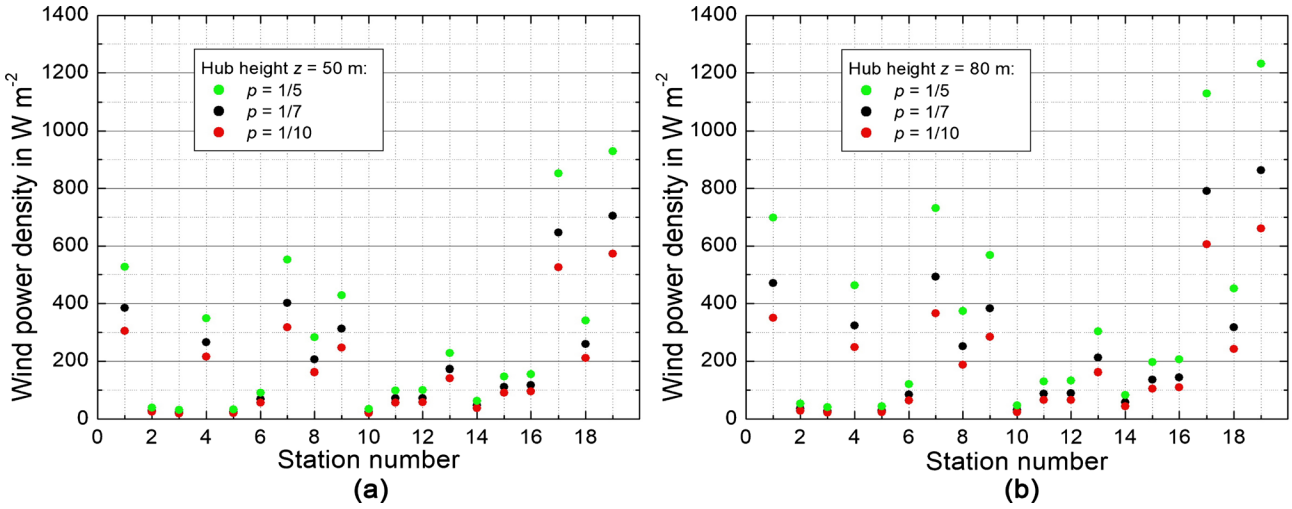

Figure 8. As in **Figure 7**, but for the mean wind-power density, $\langle S_{kin,z} \rangle$ (see Equation (2.4)) computed using daily mean wind speeds.

surrounding cities and communities, respectively. In most cases, the average trends are less then −0.0300 m·s^{-1}·a^{-1}, with exception of Gulkana that only exhibits a value of −0.0043 m·s^{-1}·a^{-1} (**Table 3**). The strongest trend occurred at Homer with −0.0500 m·s^{-1}·a^{-1}, on average, followed by Bettles with −0.0492 m·s^{-1}·a^{-1} and Yakutat with −0.0453 m·s^{-1}·a^{-1} (**Table 3**). Thus, we only discuss the predicted wind-power outcomes obtained for Barrow (1), Big Delta (4), Kotzebue (7), Nome (8), Bethel (9), King Salmon (13), Juneau (15), Annette (16), St. Paul Island (17), Kodiak (18), and Cold Bay (19) in detail. Note that Cold Bay and St. Paul Island are related to the wind-power class of 6 ("outstanding"), followed by Kotzebue that is related to a wind-power class of 4 ("good"), Barrow, Bethel and Kodiak are related to a wind-power class of 3 ("fair"), Big Delta and Nome are related to a wind-power class of 2 ("marginal"). We only considered Juneau and Annette for the purpose of comparison with recent results [15]. **Figure 9** shows the records of the daily mean wind speed at these weather stations for Period I.

The linear trends shown in **Figure 9** indicate declining trends in the daily mean wind speeds, with exception of Big Delta that shows a positive one (**Table 3**). The decrease at Barrow is marginal. At all other first-order weather stations, such declining trends in the daily mean wind speed occurred as well (**Table 3**). However, this fact is of minor importance because $\langle S_{kin,z} \rangle$ is already very low (**Figure 8**). Except for Barrow, all results are statistically significant according to a two-side t-test at 95% confidence.

We assess the impact on the sustainability of wind power by quantifying the change in the predicted wind power from Period II (January 1, 1984 to December 31, 1994) to Period III (January 1, 2006 to December 31, 2016).

3. The Impact of the Long-Term Wind-Speed Decrease on Energy Conversion at the Interface Earth-Atmosphere and Wind Power

The reasons for the long-term decrease of the mean horizontal wind speed as

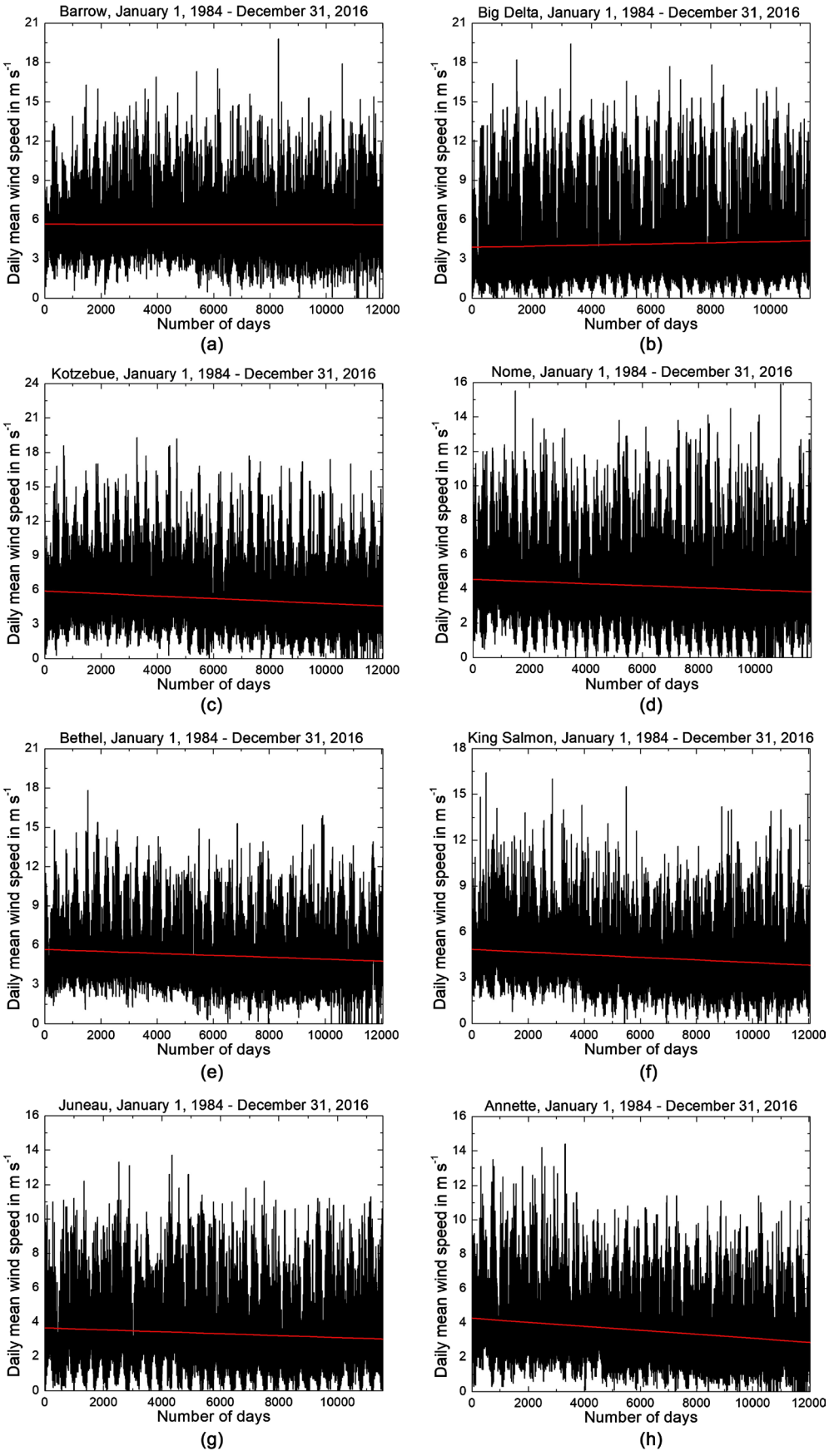
Barrow, January 1, 1984 - December 31, 2016
Daily mean wind speed in m s^{-1}
Number of days
(a)
Big Delta, January 1, 1984 - December 31, 2016
Daily mean wind speed in m s^{-1}
Number of days
(b)
Kotzebue, January 1, 1984 - December 31, 2016
Daily mean wind speed in m s^{-1}
Number of days
(c)
Nome, January 1, 1984 - December 31, 2016
Daily mean wind speed in m s^{-1}
Number of days
(d)
Bethel, January 1, 1984 - December 31, 2016
Daily mean wind speed in m s^{-1}
Number of days
(e)
King Salmon, January 1, 1984 - December 31, 2016
Daily mean wind speed in m s^{-1}
Number of days
(f)
Juneau, January 1, 1984 - December 31, 2016
Daily mean wind speed in m s^{-1}
Number of days
(g)
Annette, January 1, 1984 - December 31, 2016
Daily mean wind speed in m s^{-1}
Number of days
(h)

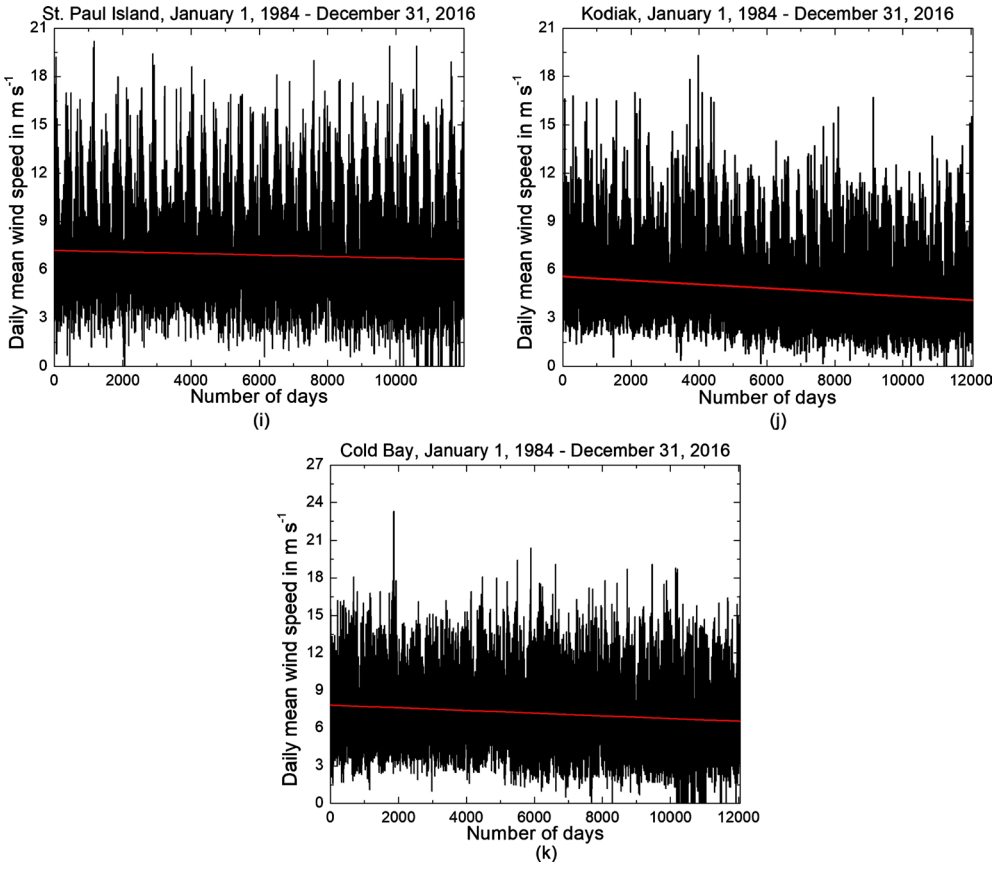

Figure 9. Records of the daily mean wind (black lines) at first-order weather stations (a) Barrow, (b) Big Delta, (c) Kotzebue, (d) Nome, (e) Bethel, (f) King Salmon, (g) Juneau, (h) Annette, (i) St. Paul Island, (j) Kodiak, and (k) Cold Bay for Period I. Red lines illustrate the linear trends (see **Table 1** for anemometer heights, z_R, at these stations).

documented by 18 of the 19 first-order weather stations in Alaska are unknown. This long-term decrease, however, may impact not only the generation of electricity using wind power, but also the near-surface air temperature. To address the latter, we considered the energy flux balance at the interface atmosphere assuming bare soil[1] for simplification. For a given location (characterized, for instance, by the zenith angle, θ, and the azimuthal angle, φ) it reads (only the components normal to the horizontal surface element play a role)

$$\begin{aligned} &R_{S\downarrow}\left(\Theta_0,\theta,\varphi\right)\left(1-\alpha_S\left(\Theta_0,\theta,\varphi\right)\right)+\varepsilon\left(\theta,\varphi\right)R_{L\downarrow}\left(\theta,\varphi\right)\\ &-\varepsilon\left(\theta,\varphi\right)\sigma T_s^4\left(\theta,\varphi\right)-H\left(\theta,\varphi\right)-E\left(\theta,\varphi\right)+G\left(\theta,\varphi\right)=0 \end{aligned} \tag{3.1}$$

Here, $R_{S\downarrow}\left(\Theta_0,\theta,\varphi\right)$ is the global (direct plus diffusive solar) radiation, $\Theta_0=\Theta_0\left(\theta,\varphi\right)$ is local zenith angle of the Sun's center, $\alpha_S\left(\Theta_0,\theta,\varphi\right)$ is the albedo of the short-wave range, $R_{L\downarrow}\left(\theta,\varphi\right)$ is the down-welling long-wave radiation, $\varepsilon\left(\theta,\varphi\right)=1-\alpha_L\left(\theta,\varphi\right)$ [64] is the relative emissivity assumed to be equal to the absorptivity, $\alpha_L\left(\theta,\varphi\right)$ is the albedo of the long-wave range, and

[1]The inclusion of a vegetation canopy has been discussed, for instance, by Deardorff [49], McCumber [50] [51], Meyers and Paw U [52] [53], Sellers *et al.* [54], Braud *et al.* [55], Kramm *et al.* [56] [57], Ziemann [58], Su *et al.* [59], Pyles *et al.* [60] [61], and Mölders *et al.* [62] [63].

$T_s(\theta,\varphi)$ is the surface temperature. The quantities $H(\theta,\varphi)$ and $E(\theta,\varphi)$ are the fluxes of sensible and latent heat within the atmosphere caused by mainly molecular effects in the immediate vicinity of the Earth's surface and by turbulent effects in the layers above. These fluxes are usually not directly measured, *i.e.*, they have to be computed based on mean quantities derived from observations. Under horizontally homogeneous and steady-state conditions these fluxes can be parameterized by [39] (hereafter, θ and φ are omitted)

$$H = -c_{p,0}\left(\overline{\rho}\alpha_T \frac{\partial \widehat{T}}{\partial z} - \overline{\rho w'' \Theta''}\right) \tag{3.2}$$

and

$$E = -\widehat{\lambda_{j1}}\left(\overline{\rho} D_{m_1} \frac{\partial \widehat{m_1}}{\partial z} - \overline{\rho w'' m_1''}\right), \tag{3.3}$$

where the vertical components of the respective gradients characterize the molecular effects in accord with the laws of Fourier and Fick, respectively, and the covariance terms $\overline{\rho w'' \Theta''}$ and $\overline{\rho w'' m_1''}$ represent the turbulent effects. Here, α_T is the thermal diffusivity, D_{m_1} is the diffusivity of the water vapor in air, and $\lambda_{j1} = h_1 - h_j$ is the specific heat of phase transition, where λ_{21} is the specific heat of vaporization, λ_{31} is the specific heat of sublimation, respectively. The fluxes of sensible and latent fluxes are usually parameterized by [39] [64]

$$H = -\overline{\rho} c_{p,0} C_h \left(U_R - U_s\right)\left(\widehat{\Theta_R} - \widehat{T_s}\right) = const. \tag{3.4}$$

and

$$E = -\overline{\rho}\,\widehat{\lambda_{k1}} C_{m_1} \left(U_R - U_s\right)\left(\widehat{m_{1,R}} - \widehat{m_{1,s}}\right) = const., \tag{3.5}$$

where horizontally homogeneous and steady-state conditions are presupposed to fulfill the requirements of the Prandtl layer (also called the atmospheric surface layer, ASL, or the constant-flux layer), the lowest layer of the atmosphere of a thickness of about ten meters. Here, $U_R = \left|\widehat{\boldsymbol{v}_R}\right|$ and $U_s = \left|\widehat{\boldsymbol{v}_s}\right|$ are the mean horizontal wind speeds at z_R (subscript R) and at the Earth's surface (subscript s), where in the case of rigid walls (like layers of soil, snow, and/or ice) the latter is equal to zero, Θ_R is the potential temperature at z_R, T_s is the absolute temperature at the water surface, and $m_{1,R}$ and $m_{1,s}$ are the corresponding values of the specific humidity. Furthermore, the potential temperature is defined by

$$\Theta = T\left(\frac{p_{a0}}{p_a}\right)^k = \frac{T}{\pi}, \tag{3.6}$$

where $\pi = \left(p_a / p_{a0}\right)^k$ is the Exner-function, p_a is the air pressure, and p_{a0} is a reference pressure (usually $p_{a0} = 1000$ hPa). The exponent k is given by

$$k = \frac{R}{c_p} \cong \frac{R_0\left\{1 + \left(R_1/R_0 - 1\right)m_1\right\}}{c_{p,0}\left\{1 + \sum_{j=1}^{3}\left(\frac{c_{p,j}}{c_{p,0}} - 1\right)m_j\right\}}. \tag{3.7}$$

Here, R is the calculated gas constant for moist air, R_0 is the calculated gas constant for dry air, R_1 is the gas constant for water vapor, $c_p = \left(\partial h/\partial T\right)_{p,m_j} = \sum_{j=0}^{3} c_{p,j} m_j$ is the specific heat at constant pressure, $c_{p,j} = \left(\partial h_j/\partial T\right)_{p,m_j}$ is the partial specific heat at constant pressure, $m_j = \rho_j/\rho$ is the mass fraction, where ρ_j is the partial density for dry air ($j=0$), water vapor ($j=1$), liquid water ($j=2$), and ice ($j=3$), respectively. These partial densities obey

$$\sum_{j=0}^{3} m_j = 1 \Rightarrow m_0 = 1 - \sum_{j=1}^{3} m_j \,. \tag{3.8}$$

Furthermore, h is the specific enthalpy, and $h_j = \left(\partial h/\partial m_j\right)_{T,p}$ is the partial specific enthalpy. Moreover, C_h and C_{m_1} are the local transfer coefficients for sensible heat and water vapor, respectively, given by

$$C_h = \frac{\kappa^2}{\left(\kappa\left(\frac{\xi_d}{2}\right)^{-\frac{1}{2}} + \ln\frac{z_R}{z_r} - \Psi_m\left(\zeta_R,\zeta_r\right)\right)\left(\kappa B_h^{-1} + \ln\frac{z_R}{z_r} - \Psi_h\left(\zeta_R,\zeta_r\right)\right)} \tag{3.9}$$

and

$$C_{m_1} = \frac{\kappa^2}{\left(\kappa\left(\frac{\xi_d}{2}\right)^{-\frac{1}{2}} + \ln\frac{z_R}{z_r} - \Psi_m\left(\zeta_R,\zeta_r\right)\right)\left(\kappa B_{m_1}^{-1} + \ln\frac{z_R}{z_r} - \Psi_{m_1}\left(\zeta_R,\zeta_r\right)\right)}, \tag{3.10}$$

where Panofsky's [65] integral similarity (or stability) functions for momentum (subscript m), sensible heat (subscript h), and water vapor (subscript m_1) are defined by (e.g., [25] [39] [66] [67])

$$\Psi_{m,h,m_1}\left(\zeta_R,\zeta_r\right) = \int_{z_r}^{z_R} \frac{1-\Phi_{m,h,m_1}\left(z/L\right)}{z}\mathrm{d}z = \int_{\zeta_r}^{\zeta_R} \frac{1-\Phi_{m,h,m_1}\left(\zeta\right)}{\zeta}\mathrm{d}\zeta \,. \tag{3.11}$$

Here, κ is the von Kármán constant, $\xi_d = 2\left(u_*/\widehat{u_r}\right)^2$ is the local drag coefficient (e.g., [68]), B_h and B_{m_1} are the sublayer Stanton number for heat and the sublayer Dalton number for water vapor, respectively (e.g., [68]-[76]), and u_* is the friction velocity defined by $u_*^2 = |\boldsymbol{\tau}|/\overline{\rho}$, where $\boldsymbol{\tau}$ is the friction stress vector. Furthermore, $\Phi_m\left(\zeta\right)$, $\Phi_h\left(\zeta\right)$, and $\Phi_{m_1}\left(\zeta\right)$ are the local similarity functions for momentum, sensible heat, and water vapor, respectively. They are based on the similarity hypothesis of Monin and Obukhov [77]. These local similarity (or stability) functions are given by

$$\Phi_m\left(\zeta\right) = \frac{z}{u_*\kappa}\left|\frac{\partial\widehat{\boldsymbol{v}_H}}{\partial z}\right| \cong \frac{z}{u_*\kappa}\frac{\partial U_H}{\partial z}, \tag{3.12}$$

$$\Phi_h\left(\zeta\right) = \frac{z}{\Theta_*\kappa}\frac{\partial\widehat{\Theta}}{\partial z}, \tag{3.13}$$

and

$$\Phi_{m_1}(\zeta)=\frac{z}{m_{1*}\kappa}\frac{\partial\widehat{m_1}}{\partial z}, \tag{3.14}$$

where $\zeta=z/L$ is the Obukhov number, $\zeta_r=z_r/L$ and $\zeta_R=z_R/L$ are the Obukhov numbers for the outer edge of the sublayer, z_r, and for the top of the Prandtl layer, z_R, and

$$L=-\frac{c_{p,0}\overline{\rho}u_*^3}{\kappa\frac{g}{\widehat{\Theta}}\left(H+0.61c_{p,0}\widehat{\Theta}\frac{E}{\widehat{\lambda_{k1}}}\right)} \tag{3.15}$$

is the Obukhov stability length. Furthermore, $c_{p,0}$ is the specific heat at constant pressure for dry air, $U_H=\left|\widehat{\boldsymbol{v}_H}\right|$ is the mean horizontal wind speed, g is the acceleration of gravity, and $\widehat{\Theta}$ is a potential temperature representative for the entire Prandtl layer.

To determine the local drag coefficient and the local similarity function for momentum, the magnitude of the friction stress vector,

$$|\boldsymbol{\tau}|=\overline{\rho}C_D\left(U_R-U_s\right)^2=const. \tag{3.16}$$

with

$$C_D=\frac{\kappa^2}{\left(\kappa\left(\frac{\xi_d}{2}\right)^{-\frac{1}{2}}+\ln\frac{z_R}{z_r}-\Psi_m\left(\zeta_R,\zeta_r\right)\right)^2} \tag{3.17}$$

and in a further step the friction velocity must be computed. Since the thermal stratification of the Prandtl layer varies in the diurnal cycle, the computation of $|\boldsymbol{\tau}|$ and u_* as well as H and E based on daily mean values of horizontal wind speed, temperature and humidity is, in general, a rather imperfect procedure. Despite the mean wind speed at the surface of rigid walls being zero, calculating of H and E over layers of bare soil, snow, and ice requires, at least, two vertical profile values of mean temperature and mean humidity, for instance, at z_R and at the surface. Since these surface values are usually unavailable, soil-vegetation-atmosphere-transfer (SVAT) schemes may be taken into consideration. Mölders *et al.* [63] [64], for instance, used the hydro-thermodynamic soil vegetation scheme (HTSVS) to predict the water budget elements (water supply to the atmosphere, groundwater recharge, and change in storage) for 2050 consecutive days (May 22, 1992 to December 31, 1997). They used routine data of hourly-mean values of horizontal wind speed, relative humidity, temperature, global radiation, and precipitation provided by a climate and lysimeter station at Brandis (south-east of Leipzig, Saxony) and evaluated the predicted water budget elements against the respective lysimeter data.

Assuming that $\hat{v}(z)$ given by Equation (2.13) is equal to

$$\hat{v}(z)=\frac{u_*}{\kappa}\left(\ln\frac{z}{z_0}-\Psi_m\left(\zeta,\zeta_0\right)\right) \tag{3.18}$$

yields [34] [78]

$$p = \ln\left\{\frac{\ln\left(\frac{z}{z_0}\right) - \Psi_m\left(\zeta,\zeta_0\right)}{\ln\left(\frac{z_R}{z_0}\right) - \Psi_m\left(\zeta_R,\zeta_0\right)}\right\}\frac{1}{\ln\left(\frac{z}{z_R}\right)}. \tag{3.19}$$

This formula shows that the shear exponent explicitly depends on thermal stratification.

Equations (3.4) and (3.5) suggest that the decrease in the mean horizontal wind speed as demonstrated by the global stilling can reduce the fluxes of sensible and latent heat, and, according to Equation (3.1), can increase the surface temperature. The situation, however, is rather complex because a decrease of evapotranspiration also affects the formation and depletion of clouds and, subsequently, the scattering and absorption of solar radiation and the emission of infrared radiation by hydrometeors. Analyzing such interrelations requires the support by non-hydrostatic models of the meso-scales β/γ [79]-[85].

Usually, MKE can be converted into TKE. In the inertial range, for instance, the TKE is transferred from lower to higher wave numbers until the far-dissipation range is reached, where kinetic energy is converted into heat energy by direct dissipation, $\overline{\boldsymbol{J}}:\nabla\hat{\boldsymbol{v}}$, and turbulent dissipation, $\overline{\boldsymbol{J}:\nabla\boldsymbol{v}''}$, where $\boldsymbol{J}$ is the Stokes stress tensor [19]. Wind turbines may generate even more TKE. Heating of air due to the dissipation of TKE has been discussed and investigated (e.g., [86] [87] [88]). It has been assessed as being marginal.

The use of wind farms, however, will contribute to a further decrease of the mean horizontal wind speed [89] [90] [91] [92] [93] and may notably affect the energy conversion at the interface Earth-atmosphere either directly as described before or indirectly, for instance, by altering the cloudiness over and/or the lee-side regions of wind-farm areas [94].

The axial momentum theory [95] [96] [97], for instance, leads to the power efficiency [19]

$$C_P = \frac{1}{2}\left(1+X\right)\left(1-X^2\right). \tag{3.20}$$

Here, $X = \widehat{v_w}/\widehat{v_\infty}$, where $\widehat{v_\infty}$ is the undisturbed wind speed far upstream of the wind turbine, and $\widehat{v_w}$ is the undisturbed wind speed far downstream of the wind turbine. This formula serves to derive the Betz-Joukowsky limit [98] [99] of $C_P = 16/27 \cong 0.593$ that occurs at $X = 1/3$. This means that, in case of this limit, the wind turbine reduces the wind speed at hub height by one third. Assuming, for instance, $\widehat{v_\infty} = 7.5\ \mathrm{m\cdot s^{-1}}$ at hub height of $z = 80\ \mathrm{m}$ would provide $\widehat{v_w} = 2.5\ \mathrm{m\cdot s^{-1}}$ at the same height. According to Equation (2.13) and a shear exponent of $p = 1/7$, such a decrease in wind speed at hub height would reduce the wind speed at the anemometer height, z_R, from nearly $\widehat{v_{\infty,R}} = 5.6\ \mathrm{m\cdot s^{-1}}$ far upstream of the wind turbine to about $\widehat{v_{w,R}} = 1.9\ \mathrm{m\cdot s^{-1}}$ far downstream of the wind turbine. The difference is $\Delta v_R = \widehat{v_{\infty,R}} - \widehat{v_{w,R}} = 3.7\ \mathrm{m\cdot s^{-1}}$. A value of $C_P = 0.45$ which is realistic for horizontal winds speed at hub height ranging

from 5 $\mathrm{m{\cdot}s^{-1}}$ to 10 $\mathrm{m{\cdot}s^{-1}}$ (Figure 11) reduces $\widehat{v_\infty} = 7.5\ \mathrm{m\cdot s^{-1}}$ at hub height of $z = 80$ m to $\widehat{v_w} = 5.1\ \mathrm{m\cdot s^{-1}}$. Using again $p = 1/7$, the wind speed $\widehat{v_w} = 5.1\ \mathrm{m\cdot s^{-1}}$ provides $\widehat{v_{w,R}} = 3.8\ \mathrm{m\cdot s^{-1}}$ and, hence, $\Delta v_R = 1.8\ \mathrm{m\cdot s^{-1}}$. The decrease of near-surface wind speeds caused by wind turbines for numerous values of the power efficiency C_P given by Equation (3.20) and the three different shear exponents $p = 1/10$, $p = 1/7$ and $p = 1/5$ are listed in Table 4. Based on these results, a notable change of the local or regional climate—depending on the size of the wind farm—is to be expected. Note that these estimates presuppose that the thermal stratification and, hence, the shear exponents are unaffected by the wind turbines. However, we must expect the interaction between the wind field, wind turbine generating vortices, and enhancing turbulence in its wake may cause that thermal stratification tends to neutral conditions.

4. The Prediction of Wind Power

The wind power is predicted based on current state-of-the-art wind turbines of different rated powers listed in Table 2 [15] [34] [35]. We discretized the power curves published by the manufacturers when other data were not available. Figure 10 illustrates the power curves of these seven wind turbines. These power curves are based on standard conditions, *i.e.*, air temperature of 15˚C, air density of 1.225 $\mathrm{kg{\cdot}m^{-3}}$, air pressure of 1013.25 hPa, and an undisturbed horizontal flow with a turbulence intensity ranging from 0.10 to 0.12. Figure 11 shows the corresponding power efficiencies.

Based on discrete power-curve data, we determined the empirical fitting parameters *A*, *K*, *Q*, *B*, *S*, and *u* of the general logistic function

$$P(v) = A + \frac{K - A}{\left(1 + Q\exp\left\{-B\left(v - S\right)\right\}\right)^{\frac{1}{u}}}, \tag{4.1}$$

where $P(v)$ represents the power generated by the respective wind turbine at the wind speed *v* at hub height. The parameters obtained are listed in Table 5.

Table 4. The decrease of near-surface wind speed caused by wind turbines for numerous values of the power efficiency, C_P, given by Equation (3.20) and the shear exponents, *p*, used in this study. A horizontal wind speed of $\widehat{v_\infty} = 7.5\ \mathrm{m\cdot s^{-1}}$ at hub height of $z = 80$ m was assumed.

$X = \widehat{v_w}/\widehat{v_\infty}$	C_p	$\widehat{v_{\infty,R}}\left(\mathrm{m\cdot s^{-1}}\right)$			$\Delta v_R = \widehat{v_{\infty,R}} - \widehat{v_{w,R}}\left(\mathrm{m\cdot s^{-1}}\right)$		
		$p = 1/10$	$p = 1/7$	$p = 1/5$	$p = 1/10$	$p = 1/7$	$p = 1/5$
0.333	0.593	6.1	5.6	4.9	4.1	3.7	3.3
0.618	0.500				2.3	2.1	1.9
0.682	0.450				1.9	1.8	1.6
0.733	0.400				1.6	1.5	1.3
0.778	0.350				1.3	1.2	1.1
0.818	0.300				1.1	1.0	0.9

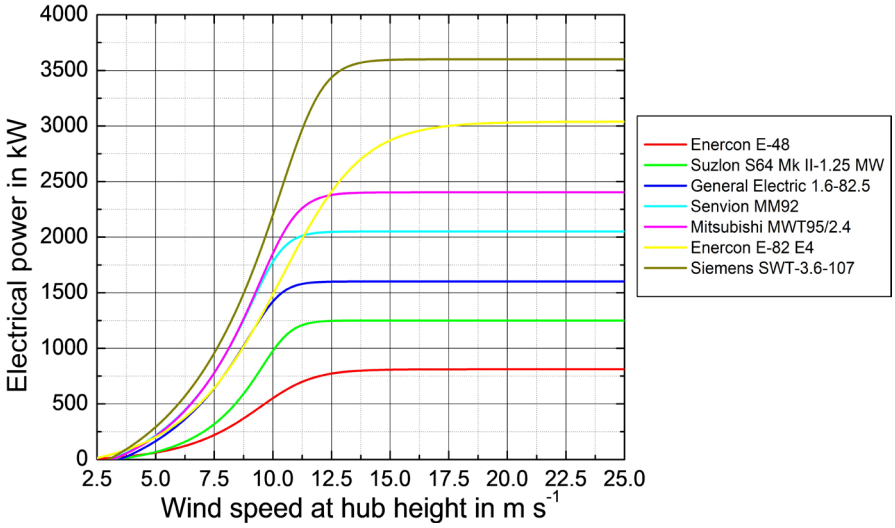

Figure 10. Power curves of the seven wind turbines listed in **Table 2** (adopted from [19]).

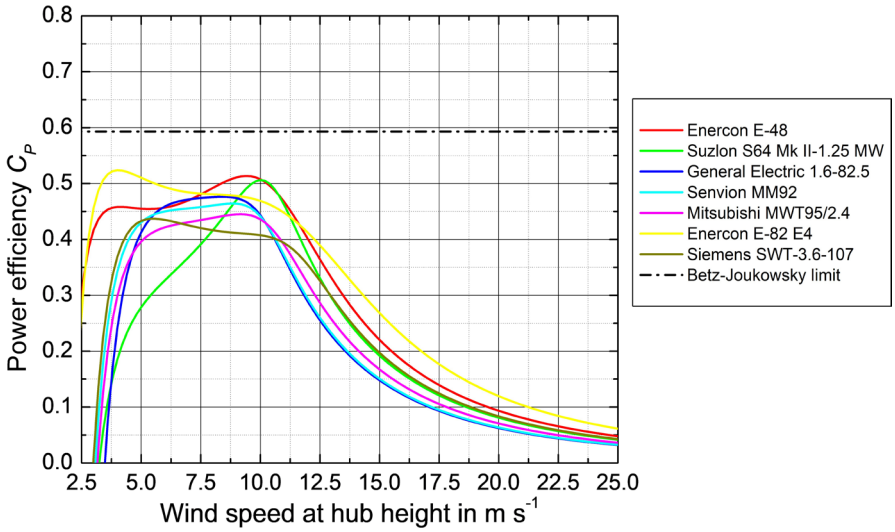

Figure 11. Power efficiencies of the seven wind turbines listed in **Table 2** (adopted from [19]).

Table 5. Parameters used in the generalized logistic function, Equation (4.1), to model the turbines' power curves. Values for Senvion MM92 and Mitsubishi MWT95/2.4 are from Ross *et al.* [34], the others are from Kramm *et al.* [19]

Wind turbine	A	K	Q	B	S	u
Enercon E-48	−24.9	811.2	0.54	1.0	10.9	2.3
Suzlon S64 Mark II -1.25 MW	−56.5	1250.6	3.88	2.0	9.6	4.5
General Electric 1.6-82.5	−315.7	1601.3	1.66	2.0	9.8	7.2
Senvion MM92	−267.6	2050.4	19.5	1.9	8.5	6.2
Mitsubishi MWT95/2.4	−270.4	2403.3	12.2	1.5	8.8	4.9
Enercon E-82 E4	−113.8	3038.8	1.49	0.6	10.6	1.7
Siemens SWT-3.6-107	−414.3	3599.6	40.0	1.4	9.0	5.4

For each period, we calculated the average power output by

$$\langle P_{WT} \rangle = \int_{v_{ci}}^{v_{co}} f(v) P(v) \mathrm{d}v . \tag{4.2}$$

Here, v_{ci} is the cut-in wind speed, v_{co} is the cut-out wind speed, and $f(v)$ is the probability density function of a given horizontal wind speed at hub height, v, occurring during a period. It is expressed by the Weibull two-parameter distribution [100],

$$f(v)\mathrm{d}v = \frac{k_W}{c_W}\left(\frac{v}{c_W}\right)^{k_W-1} \exp\left(-\left(\frac{v}{c_W}\right)^{k_W}\right)\mathrm{d}v , \tag{4.3}$$

where k_W and c_W represent the shape and scale parameters, respectively (e.g., [16] [70] [71]). The scale factor has units of speed and is closely related to the mean wind speed at hub height. The shape parameter is a non-dimensional quantity inversely related to the variance of the wind speed [101]. The integration of Equation (4.3) leads to the cumulative distribution function [100]

$$F(v) = 1 - \exp\left(-\left(\frac{v}{c_W}\right)^{k_W}\right), \tag{4.4}$$

where $F(v) \to 1$ for $v \to \infty$. The shape and scale parameters are determined for each of Alaska's 19 first-order weather stations for Period I by fitting the histograms of the normalized cumulative frequency of the predicted wind speeds at the hub height $z = 80$ m using the three different shear exponents, $p = 1/10$, $p = 1/7$ and $p = 1/5$. For Barrow, Big Delta, Kotzebue, Nome, Bethel, King Salmon, Juneau, Annette, St. Paul Island, Kodiak, and Cold Bay, k_W and c_W were also determined for Periods II and III. **Figure 12** exemplarily

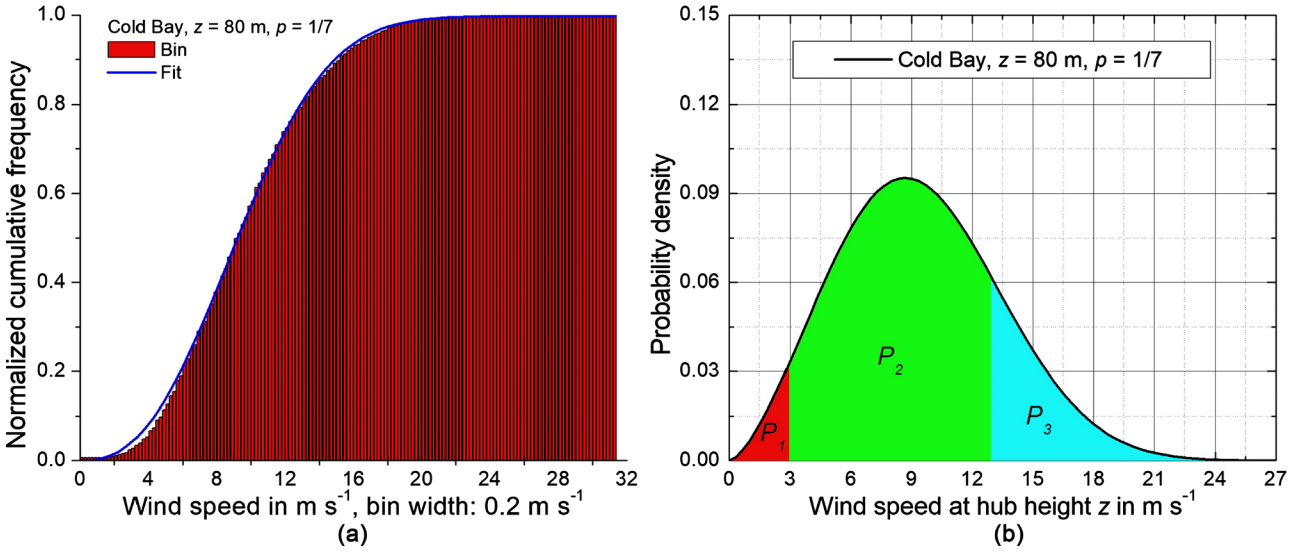

Figure 12. (a) Fitted normalized cumulative frequency and (b) probability density function of the predicted wind speeds at the hub height $z = 80$ m as obtained for Cold Bay using a shear exponent of $p = 1/7$. The probabilities P_1, P_2, and P_3 that the daily mean wind speed will be in one of these colored areas are defined by Equations (4.5) to (4.7).

shows both the fitted normalized cumulative frequency for Period I and the corresponding Weibull distribution at hub height obtained for Cold Bay using $p = 1/7$. The results are listed in Table 6. Obviously, the scale parameters obtained for Periods II and III also indicate the near-surface wind-speed stilling, with exception of Barrow and Big Delta.

The probability that the daily mean wind speed does not meet the cut-in speed requirements of the different wind turbines considered in this study is given by

$$P_1 = P\left[0, v_{ci}\right) = F\left(v_{ci}\right). \tag{4.5}$$

Furthermore, the probability that the daily mean wind speed is in the range between v_{ci} and the wind speed of the rated power, v_{pr}, is given by

$$P_2 = P\left[v_{ci}, v_{pr}\right) = F\left(v_{pr}\right) - F\left(v_{ci}\right). \tag{4.6}$$

The probability that the daily mean wind speed exceeds v_{pr} results in

$$P_3 = P\left[v_{pr}, v_{\max}\right) = F\left(v_{\max}\right) - F\left(v_{pr}\right), \tag{4.7}$$

where $F\left(v_{\max}\right) \cong 1$ for the maximum value $v_{\max}$ of the daily mean wind speed. For the purpose of simplification, a common cut-in wind speed of $v_{ci} = 3.0\ \mathrm{m \cdot s^{-1}}$ and a common wind speed of the rated power of $v_{pr} = 13.0\ \mathrm{m \cdot s^{-1}}$ are assumed. Both wind speeds are averages derived from the wind turbine specifications (Table 2). The sum $P_2 + P_3$ broadly coincides with the operating range of a modern wind turbine.

The ratio of the average power output, $\langle P_{WT} \rangle$, provided by a wind turbine to its rated power, P_R, is the capacity factor

$$C_F = \frac{\langle P_{WT} \rangle}{P_R}. \tag{4.8}$$

The capacity factor may empirically be related to the ratio $R_P = P_3 / \left(P_2 + P_3\right)$.

5. Results

5.1. Hourly Mean Wind Speeds versus Daily Mean Wind Speeds

Because of Inequality (2.8), we must expect that hourly mean wind speeds provide higher wind-power outputs than daily mean wind speeds. To estimate possible deviations, we used (a) the hourly mean wind speeds and (b) daily mean wind speeds both related to the wind speed measurements at anemometer height $z_R = 8\ \mathrm{m}\left(26\ \mathrm{ft}\right)$ at Bethel performed from January 1, 1979 to December 31, 1983. Results obtained at $z = 80\ \mathrm{m}$ are illustrated in Figure 13 and Figure 14, where, again, $p = 1/10$, $p = 1/7$ and $p = 1/5$ were used.

Figure 13 shows the probability density functions of (a) the hourly mean wind speeds and (b) the daily mean wind speeds at the hub height. Obviously, these probability density functions remarkably differ so that—according to Equation (4.2)—different amounts of wind power were predicted for each of the seven wind turbines considered. Figure 14 shows the predicted wind power, $\langle P_{WT,h} \rangle$, obtained from the hourly mean wind speeds and the corresponding

Table 6. Weibull shape and scale parameters deduced from the predicted wind speeds at hub height of $z = 80$ m for Alaska's 19 first-order weather stations using three different shear exponents, $p = 1/10$, $p = 1/7$ and $p = 1/5$. Predicted wind speeds are based on the daily mean wind speeds at the respective anemometer heights for Periods I, II, and III.

Location	Period	Shape parameter k_w			Scale parameter c_w (m·s^{-1})		
		Shear exponent p					
		1/10	1/7	1/5	1/10	1/7	1/5
Barrow WSO	I	2.451	2.458	2.460	7.568	8.362	9.554
	II	2.683	2.708	2.703	7.517	8.326	9.505
	III	2.267	2.269	2.272	7.444	8.237	9.409
Bettles	I	2.289	2.306	2.270	3.373	3.686	4.151
Fairbanks INTL	I	1.707	1.715	1.698	2.803	3.062	3.442
Big Delta FAA/AMOS	I	1.274	1.280	1.212	5.178	5.657	6.154
	II	1.141	1.140	1.154	4.892	5.206	6.026
	III	1.349	1.338	1.346	5.229	5.830	6.450
McGrath	I	1.702	1.711	1.694	2.902	3.170	3.566
Gulkana	I	1.190	1.188	1.185	3.385	3.681	4.149
Kotzebue WSO	I	1.868	1.889	1.889	6.994	7.763	8.865
	II	2.094	2.102	2.100	7.591	8.400	9.594
	III	1.688	1.692	1.693	6.397	7.083	8.091
Nome WSO	I	1.873	1.880	1.879	5.753	6.374	7.279
	II	2.132	2.063	2.076	5.938	6.504	7.438
	III	1.693	1.700	1.701	5.393	5.972	6.825
Bethel	I	2.443	2.452	2.449	6.990	7.736	8.835
	II	2.714	2.718	2.561	7.520	8.312	9.371
	III	2.290	2.276	2.294	6.719	7.423	8.495
Talkeetna	I	1.710	1.716	1.722	2.757	3.062	3.502
Anchorage INTL	I	2.295	2.306	2.315	4.146	4.596	5.253
Homer	I	2.247	2.248	2.257	4.213	4.669	5.334
King Salmon	I	2.271	2.276	2.277	5.685	6.223	7.016
	II	2.675	2.805	2.686	6.276	6.968	7.741
	III	2.031	2.065	2.041	5.369	5.903	6.637
Yakutat	I	1.733	1.741	1.725	3.394	3.706	4.176
Juneau	I	1.556	1.554	1.552	4.458	4.862	5.491
	II	1.700	1.693	1.721	4.760	5.195	5.887
	III	1.424	1.424	1.421	4.097	4.465	5.049
Annette WSO	I	1.797	1.783	1.795	4.657	5.069	5.743
	II	2.052	2.050	2.114	5.183	5.663	6.468
	III	1.624	1.624	1.618	4.056	4.421	4.995

Continued

	I	2.449	2.450	2.462	9.235	10.103	11.396
St. Paul Island	II	2.610	2.593	2.610	9.400	10.273	11.587
	III	2.278	2.278	2.287	8.989	9.839	11.093
	I	2.055	2.113	2.058	6.306	6.959	7.777
Kodiak	II	2.386	2.378	2.392	7.003	7.656	8.635
	III	1.898	1.900	1.906	5.764	6.304	7.177
	I	2.507	2.510	2.508	9.725	10.641	11.989
Cold Bay	II	2.705	2.710	2.706	10.118	11.069	12.470
	III	2.358	2.360	2.362	9.289	10.165	11.455

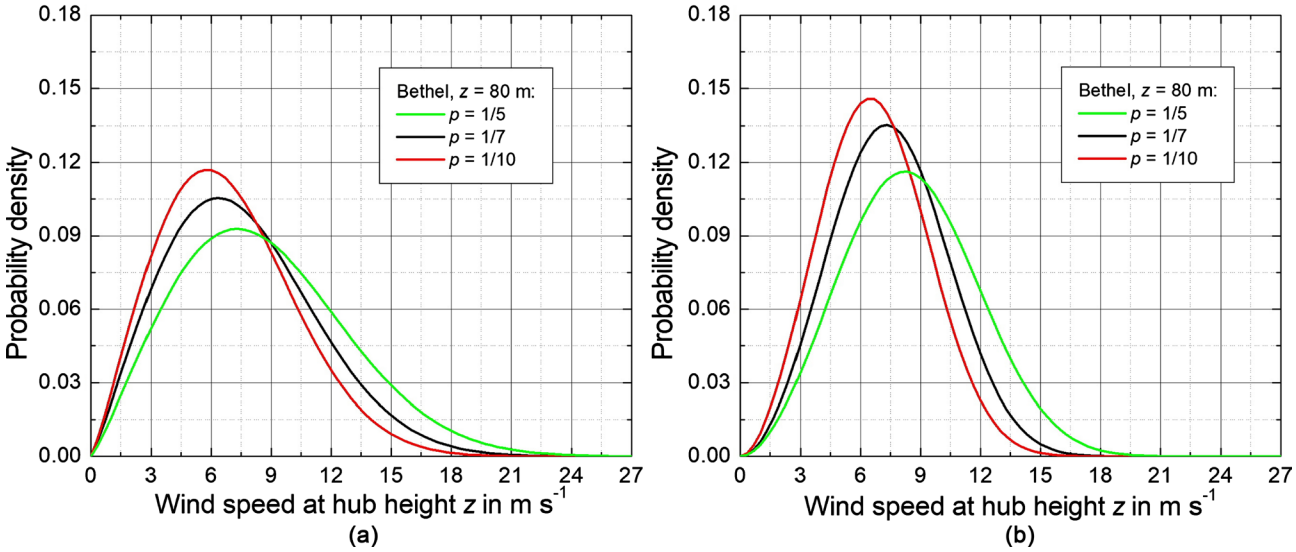

Figure 13. Probability density functions at hub height of $z = 80$ m derived from (a) hourly mean wind speeds and (b) daily mean wind speeds both using wind speed measurements performed at the anemometer height $z_R = 8\,\text{m}\,(26\,\text{ft})$ in Bethel during January 1, 1979 to December 31, 1983 for $p = 1/10$, $p = 1/7$ and $p = 1/5$.

capacity factor, $C_{F,h}$. As expected, we obtained for $p = 1/5$ (stable stratification) always the highest values of $\langle P_{WT,h} \rangle$ and $C_{F,h}$ for each wind turbine, followed by those for $p = 1/7$ (neutral stratification) and $p = 1/10$ (unstable stratification). The General Electric 1.6 - 82.5 and Senvion MM92 have the highest and second highest capacity factor, respectively. This result agrees with that of Mölders *et al.* [15].

Figure 14 shows the relative differences between $\langle P_{WT,h} \rangle$ and that based on the daily mean wind speeds, $\langle P_{WT,d} \rangle$, expressed by

$$\Delta P_{WT,h} = \frac{\langle P_{WT,h} \rangle - \langle P_{WT,d} \rangle}{\langle P_{WT,h} \rangle}. \tag{5.1}$$

For $p = 1/10$ this relative difference is always positive, *i.e.*, the predicted wind power based on hourly mean wind speeds always exceeds that calculated with daily mean wind speeds. For the shear exponents $p = 1/7$ and $p = 1/5$,

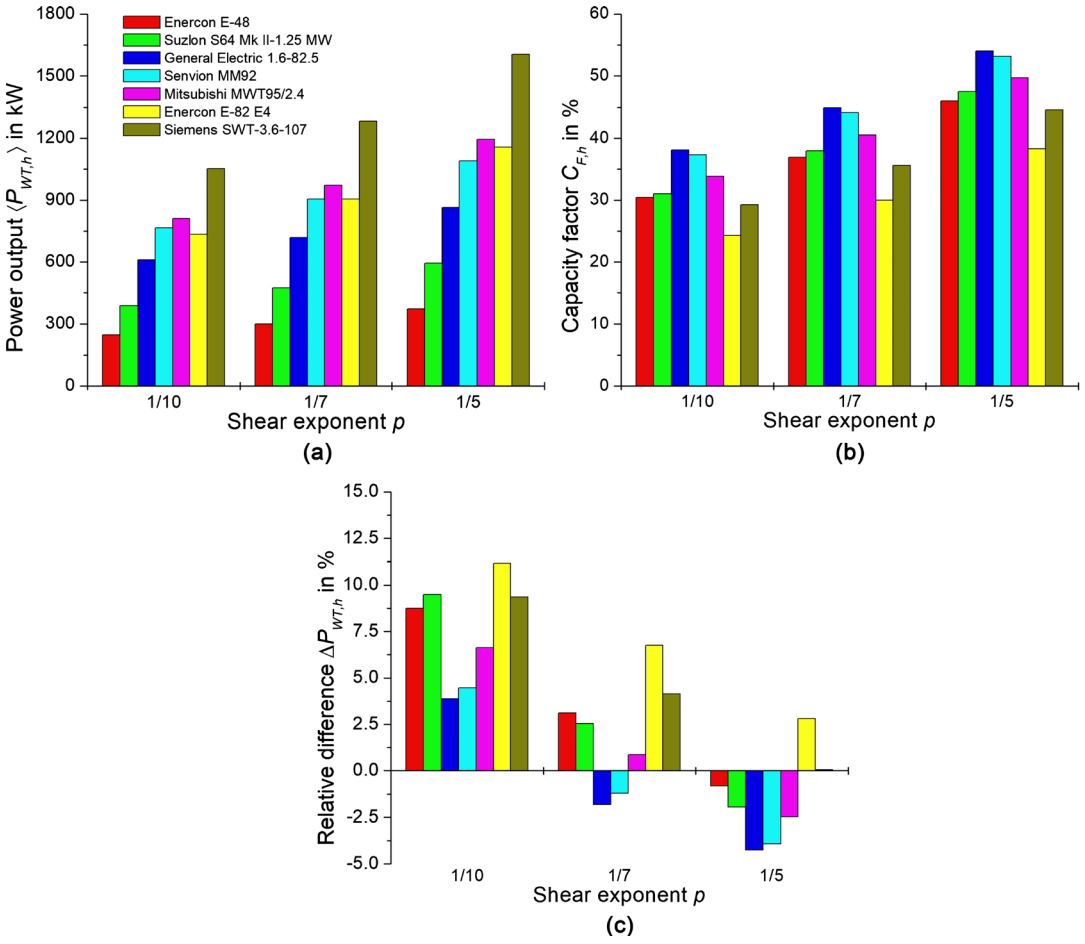

Figure 14. As in **Figure 13**, but for (a) the predicted wind power, $\langle P_{WT,h} \rangle$, (b) the corresponding capacity factor, $C_{F,h}$, and (c) relative difference $\Delta P_{WT,h}$ as expressed by Equation (5.1).

however, positive as well as negative values of ΔP_{WT} occur. Negative values can be attributed to the fitted curves of the normalized frequencies in case of the daily mean wind speeds. In contrast to the case of the hourly mean wind speeds, these fitted curves slightly overestimated the normalized frequencies in the range from 9 m·s^{-1} to 15 m·s^{-1}. Thus, we must expect that for the same period, hourly mean wind speeds provide slightly higher average wind-power outputs, $\langle P_{WT,h} \rangle$, than daily mean wind speeds, $\langle P_{WT,d} \rangle$.

5.2. Daily Mean Wind Speeds

Our predicted wind power obtained for Barrow, Big Delta, Kotzebue, Nome, Bethel, King Salmon, Juneau, St. Paul Island, Kodiak, and Cold Bay for Periods I, II, and III using $p = 1/10$, $p = 1/7$ and $p = 1/5$, is listed in **Table 7**. The effect of the shear exponent on the probability density function and the wind-power output predicted for Periods I, II, and III is exemplarily shown in **Figure 15** to **Figure 17** for Cold Bay.

Figure 15 and **Figure 16** show the results obtained for the seven wind turbines of different rated power (see **Table 2**). Generally, the power output predicted at

Table 7. Wind power predicted for first-order weather stations Barrow, Big Delta, Kotzebue, Nome, Bethel, King Salmon, Juneau, Annette, St. Paul Island, Kodiak, and Cold Bay and Periods I, II, and III using $p = 1/10$, $p = 1/7$ and $p = 1/5$.

Weather station	p	Period	Wind turbine						
			E-48 (kW)	S64 Mk II-1.25 MW (kW)	GE 1.6-82.5 (kW)	MM92 (kW)	MWT95/2.4 (kW)	E-82E4 (kW)	SWT-3.6-107 (kW)
Barrow WSO	1/10	I	230	360	584	731	766	672	977
		II	222	346	574	717	745	643	940
		III	225	352	566	710	746	662	958
	1/7	I	287	456	707	887	943	848	1221
		II	282	450	708	887	937	826	1199
		III	279	443	683	858	915	833	1192
	1/5	I	367	589	869	1094	1188	1117	1575
		II	368	592	881	1108	1197	1104	1573
		III	355	567	836	1054	1145	1087	1525
Big Delta FAA/AMOS	1/10	I	138	211	333	421	448	422	592
		II	135	207	321	406	436	418	581
		III	135	205	328	414	438	409	577
	1/7	I	162	250	387	488	524	500	697
		II	151	232	355	448	484	468	648
		III	167	258	400	505	541	514	718
	1/5	I	191	296	445	560	610	597	821
		II	187	291	435	548	598	590	808
		III	199	309	468	590	639	616	855
Kotzebue WSO	1/10	I	207	322	510	642	680	619	885
		II	239	375	589	740	785	711	1019
		III	178	275	439	553	585	535	763
	1/7	I	254	400	612	771	827	770	1089
		II	291	461	700	881	947	880	1247
		III	219	341	528	665	711	664	938
	1/5	I	318	504	744	938	1022	986	1371
		II	363	577	842	1062	1161	1125	1562
		III	276	434	647	816	886	854	1186
Nome WSO	1/10	I	130	194	335	422	435	385	557
		II	130	192	340	428	437	382	555
		III	119	178	304	383	396	355	510
	1/7	I	168	257	423	532	556	497	716
		II	168	257	430	540	561	495	717
		III	152	232	381	480	503	455	651
	1/5	I	224	351	549	690	734	674	960

Continued

		II	229	359	568	713	755	681	978
		III	203	316	495	623	663	614	870
Bethel	1/10	I	189	290	490	613	634	550	803
		II	221	345	574	717	744	642	939
		III	175	266	452	567	585	510	743
	1/7	I	242	380	611	765	804	709	1028
		II	281	448	706	884	933	823	1194
		III	223	349	563	706	741	657	950
	1/5	I	320	510	774	973	1044	956	1365
		II	357	573	853	1074	1160	1075	1527
		III	296	471	720	905	969	888	1267
King Salmon	1/10	I	110	157	293	368	372	325	472
		II	134	195	363	454	458	395	576
		III	101	144	266	336	340	300	434
	1/7	I	142	212	375	470	480	418	608
		II	179	271	476	594	607	519	761
		III	131	193	340	428	438	384	558
	1/5	I	195	301	500	626	652	572	830
		II	238	374	612	765	798	693	1012
		III	178	273	451	567	591	524	758
Juneau	1/10	I	79	112	202	256	261	235	337
		II	85	121	220	279	284	254	364
		III	71	101	179	228	233	212	302
	1/7	I	100	146	252	319	329	297	425
		II	109	160	277	350	360	322	463
		III	89	130	223	283	292	265	379
	1/5	I	134	203	333	421	441	401	573
		II	146	222	368	463	484	435	625
		III	119	179	295	373	391	359	510
Annette WSO	1/10	I	75	104	195	248	251	224	322
		II	91	126	239	302	304	269	388
		III	57	76	146	187	187	171	243
	1/7	I	97	139	250	316	322	287	413
		II	117	171	306	386	393	345	500
		III	73	102	188	239	242	218	312
	1/5	I	134	201	341	429	445	396	571
		II	164	249	422	530	548	482	699

Continued

		III	102	150	261	329	339	304	437
St. Paul Island	1/10	I	347	555	828	1042	1125	1046	1483
		II	360	577	861	1083	1169	1081	1537
		III	329	524	785	988	1067	996	1409
	1/7	I	401	643	933	1176	1287	1236	1725
		II	416	668	966	1219	1334	1277	1786
		III	381	609	886	1118	1222	1176	1639
	1/5	I	472	755	1062	1342	1491	1495	2041
		II	489	783	1098	1389	1544	1548	2115
		III	448	715	1011	1276	1417	1420	1938
Kodiak	1/10	I	156	236	401	504	521	459	665
		II	191	294	494	619	641	558	813
		III	130	193	334	421	433	383	554
	1/7	I	196	304	496	623	652	579	837
		II	237	373	598	750	788	697	1010
		III	163	248	411	517	539	481	693
	1/5	I	252	396	615	774	824	754	1076
		II	306	487	744	934	1000	914	1306
		III	217	339	534	672	713	650	928
Cold Bay	1/10	I	379	608	894	1126	1224	1154	1626
		II	409	659	959	1209	1318	1246	1754
		III	349	558	828	1043	1129	1060	1496
	1/7	I	434	697	997	1258	1385	1351	1872
		II	466	749	1063	1343	1483	1453	2010
		III	402	644	930	1174	1287	1246	1731
	1/5	I	502	802	1116	1411	1577	1608	2176
		II	535	855	1181	1494	1675	1721	2321
		III	469	749	1052	1329	1480	1494	2031

hub height for each of these weather stations non-linearly depends on the shear exponent of the power law (see Equation (2.13)). For $p = 1/10$, each wind turbine provides the lowest wind-power output. Whereas the opposite is true in case of $p = 1/5$. Consequently, the capacity factor for each wind turbine is the lowest for $p = 1/10$ and the highest for $p = 1/5$ (see **Table 8**).

Based on the capacity factors for Period I, Cold Bay, St. Paul Island, Barrow, Bethel, and Kotzebue would be very good candidates for wind farms, as already found by Cooney and Kramm [105] for a short period, but Cold Bay and St. Paul Island changed their ranks. At Kodiak, Nome, King Salmon, and Big Delta, wind-power generation may be considered for the reduction of fossil fuel consumption. In

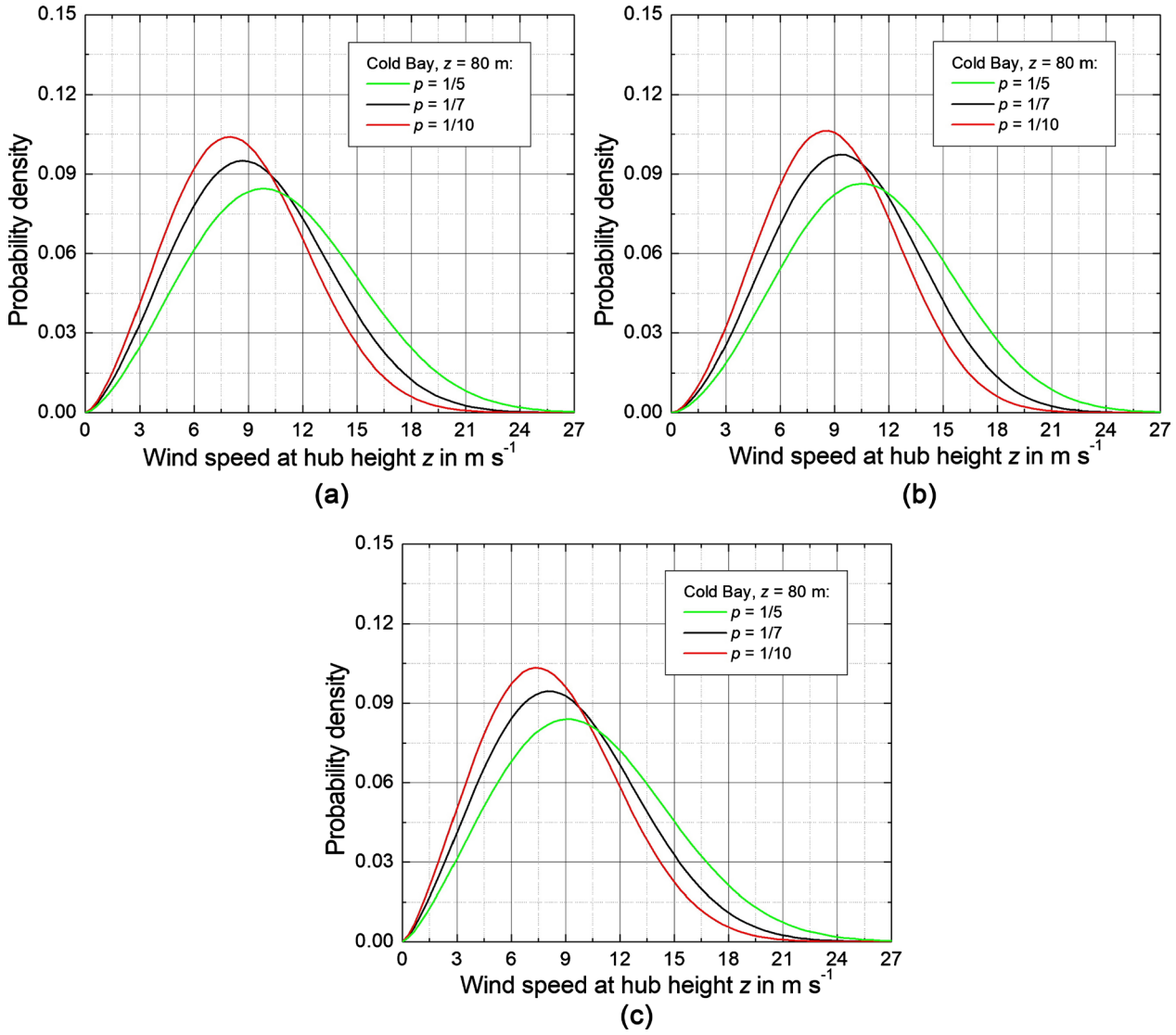

Figure 15. Probability density functions at the hub height of $z = 80$ m for (a) Period I, (b) Period II, and (c) Period III determined for Cold Bay from the daily mean wind speeds related to the wind-speed measurements performed at the anemometer height $z_R = 10$ m$(33$ ft$)$ using $p = 1/10$, $p = 1/7$ and $p = 1/5$.

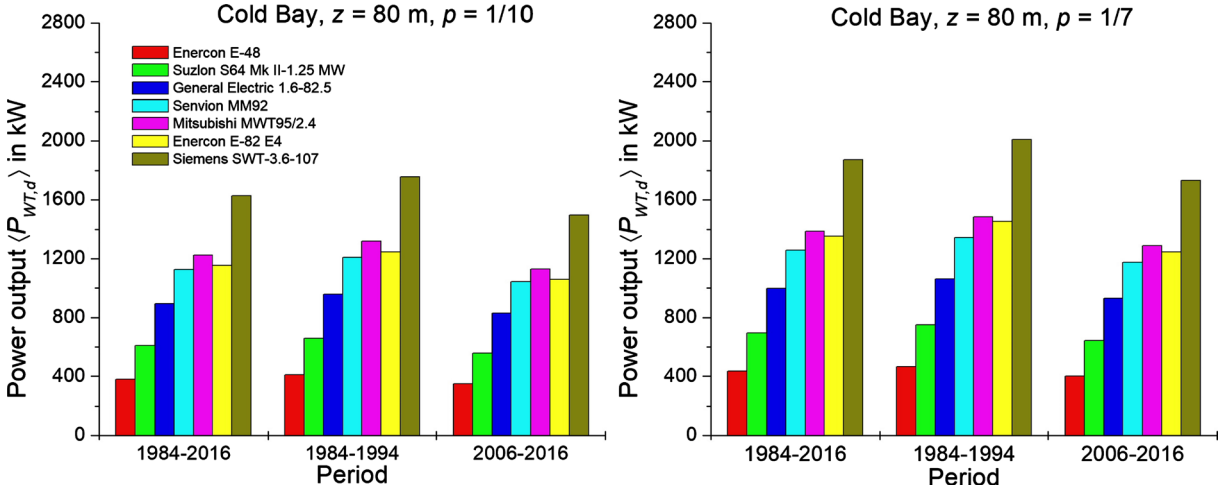

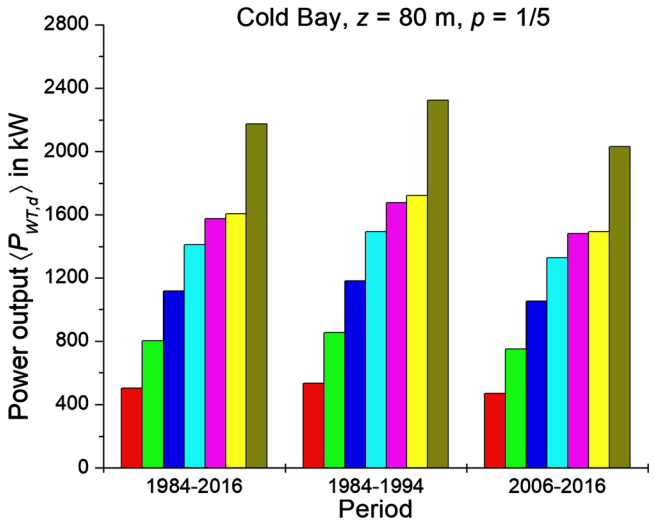

Figure 16. Predicted wind-power output $\langle P_{WT,d} \rangle$ at hub height $z = 80$ m for Cold Bay using seven wind turbines of different rated power (**Table 2**) as well as $p = 1/10$, $p = 1/7$, and $p = 1/5$.

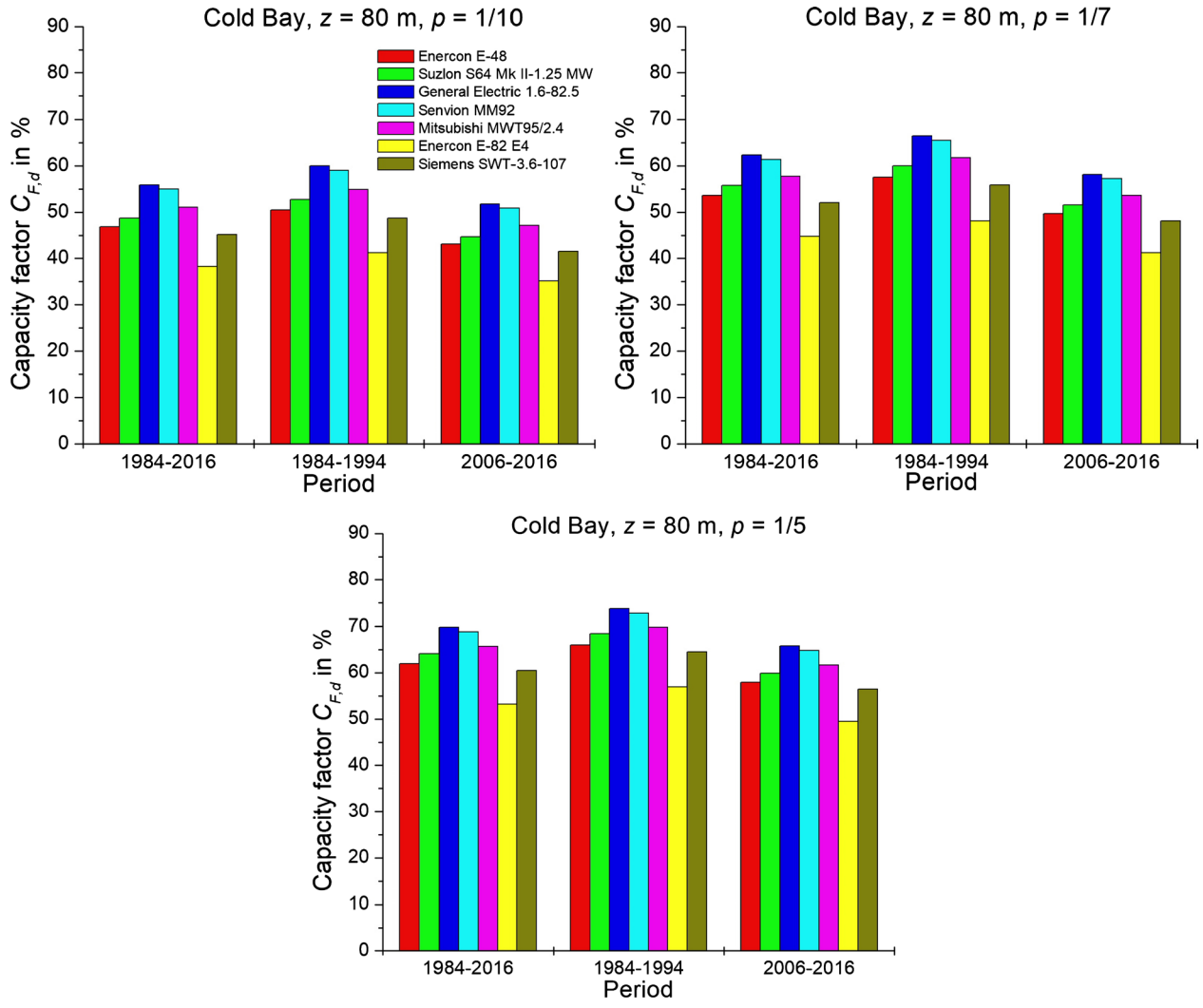

Figure 17. As in **Figure 16**, but for the predicted capacity factor $C_{F,d}$.

Table 8. As in **Table 7**, but for the capacity factor.

Weather station	p	Period	Wind turbine						
			E-48 (%)	S64 Mk II-1.25 MW (%)	GE 1.6-82.5 (%)	MM92 (%)	MWT95/2.4 (%)	E-82E4 (%)	SWT-3.6-107 (%)
Barrow WSO	1/10	I	28.4	28.8	36.5	35.7	31.9	22.3	27.1
		II	27.4	27.6	35.9	35.0	31.0	21.3	26.1
		III	27.8	28.1	35.4	34.6	31.1	21.9	26.6
	1/7	I	35.4	36.4	44.2	43.3	39.3	28.1	33.9
		II	34.9	36.0	44.3	43.3	39.0	27.4	33.3
		III	34.5	35.4	42.7	41.9	38.1	27.6	33.1
	1/5	I	45.4	47.1	54.3	53.4	49.5	37.0	43.8
		II	45.4	47.4	55.1	54.1	49.9	36.6	43.7
		III	43.8	45.4	52.3	51.4	47.7	36.0	42.4
Big Delta FAA/AMOS	1/10	I	17.0	16.9	20.8	20.5	18.7	14.0	16.5
		II	16.7	16.6	20.1	19.8	18.2	13.8	16.1
		III	16.6	16.4	20.5	20.2	18.3	13.5	16.0
	1/7	I	20.0	20.0	24.2	23.8	21.8	16.6	19.4
		II	18.6	18.5	22.2	21.9	20.1	15.5	18.0
		III	20.6	20.6	25.0	24.6	22.5	17.0	20.0
	1/5	I	23.5	23.7	27.8	27.3	25.4	19.8	22.8
		II	23.1	23.3	27.2	26.7	24.9	19.5	22.5
		III	24.5	24.7	29.3	28.8	26.6	20.4	23.7
Kotzebue WSO	1/10	I	25.5	25.7	31.9	31.3	28.3	20.5	24.6
		II	29.5	30.0	36.8	36.1	32.7	23.5	28.3
		III	22.0	22.0	27.5	27.0	24.4	17.7	21.2
	1/7	I	31.4	32.0	38.3	37.6	34.4	25.5	30.2
		II	35.9	36.9	43.7	43.0	39.5	29.2	34.6
		III	27.0	27.3	33.0	32.4	29.6	22.0	26.0
	1/5	I	39.3	40.3	46.5	45.8	42.6	32.7	38.1
		II	44.8	46.2	52.6	51.8	48.4	37.3	43.4
		III	34.0	34.7	40.5	39.8	36.9	28.3	33.0
Nome WSO	1/10	I	16.1	15.5	20.9	20.6	18.1	12.8	15.5
		II	16.1	15.3	21.3	20.9	18.2	12.7	15.4
		III	14.7	14.2	19.0	18.7	16.5	11.7	14.2
	1/7	I	20.7	20.5	26.4	25.9	23.2	16.5	19.9
		II	20.8	20.5	26.9	26.4	23.4	16.4	19.9
		III	18.8	18.6	23.8	23.4	21.0	15.1	18.1
	1/5	I	27.7	28.0	34.3	33.7	30.6	22.3	26.7

Continued

		II	28.3	28.7	35.5	34.8	31.4	22.6	27.2
		III	25.1	25.3	30.9	30.4	27.6	20.3	24.2
Bethel	1/10	I	23.3	23.2	30.6	29.9	26.4	18.2	22.3
		II	27.3	27.6	35.9	35.0	31.0	21.3	26.1
		III	21.5	21.3	28.3	27.6	24.4	16.9	20.6
	1/7	I	29.9	30.4	38.2	37.3	33.5	23.5	28.6
		II	34.7	35.8	44.1	43.1	38.9	27.2	33.2
		III	27.6	27.9	35.2	34.4	30.9	21.7	26.4
	1/5	I	39.5	40.8	48.4	47.5	43.5	31.6	37.9
		II	44.1	45.8	53.3	52.4	48.3	35.6	42.4
		III	36.6	37.7	45.0	44.1	40.4	29.4	35.2
King Salmon	1/10	I	13.6	12.5	18.3	18.0	15.5	10.8	13.1
		II	16.6	15.6	22.7	22.1	19.1	13.1	16.0
		III	12.5	11.5	16.6	16.4	14.2	9.9	12.0
	1/7	I	17.6	16.9	23.4	22.9	20.0	13.8	16.9
		II	22.1	21.7	29.8	29.0	25.3	17.2	21.1
		III	16.1	15.5	21.3	20.9	18.3	12.7	15.5
	1/5	I	24.1	24.1	31.2	30.5	27.2	18.9	23.1
		II	29.4	30.0	38.2	37.3	33.3	23.0	28.1
		III	21.9	21.8	28.2	27.7	24.6	17.4	21.0
Juneau	1/10	I	9.7	9.0	12.6	12.5	10.9	7.8	9.4
		II	10.5	9.7	13.7	13.6	11.8	8.4	10.1
		III	8.7	8.1	11.2	11.1	9.7	7.0	8.4
	1/7	I	12.3	11.7	15.8	15.6	13.7	9.8	11.8
		II	13.4	12.8	17.3	17.1	15.0	10.7	12.9
		III	10.9	10.4	13.9	13.8	12.2	8.8	10.5
	1/5	I	16.5	16.2	20.8	20.5	18.4	13.3	15.9
		II	18.1	17.7	23.0	22.6	20.2	14.4	17.4
		III	14.7	14.4	18.4	18.2	16.3	11.9	14.2
Annette WSO	1/10	I	9.3	8.3	12.2	12.1	10.4	7.4	8.9
		II	11.2	10.1	14.9	14.7	12.7	8.9	10.8
		III	7.0	6.1	9.1	9.1	7.8	5.6	6.7
	1/7	I	11.9	11.1	15.6	15.4	13.4	9.5	11.5
		II	14.4	13.6	19.1	18.8	16.4	11.4	13.9
		III	9.0	8.2	11.7	11.6	10.1	7.2	8.7
	1/5	I	16.5	16.0	21.3	20.9	18.5	13.1	15.9
		II	20.3	19.9	26.4	25.8	22.8	16.0	19.4

Continued

		III	12.6	12.0	16.3	16.1	14.1	10.1	12.1
St. Paul Island	1/10	I	42.8	44.4	51.7	50.8	46.9	34.6	41.2
		II	44.4	46.2	53.8	52.8	48.7	35.8	42.7
		III	40.6	42.0	49.0	48.2	44.4	33.0	39.1
	1/7	I	49.5	51.4	58.3	57.4	53.6	40.9	47.9
		II	51.3	53.4	60.4	59.5	55.6	42.3	49.6
		III	47.0	48.7	55.4	54.5	50.9	39.0	45.5
	1/5	I	58.2	60.4	66.4	65.5	62.1	49.5	56.7
		II	60.3	62.7	68.7	67.7	64.3	51.3	58.7
		III	55.3	57.2	63.2	62.3	59.0	47.0	53.8
Kodiak	1/10	I	19.3	18.9	25.1	24.6	21.7	15.2	18.5
		II	23.6	23.5	30.9	30.2	26.7	18.5	22.6
		III	16.0	15.5	20.9	20.5	18.1	12.7	15.4
	1/7	I	24.2	24.3	31.0	30.4	27.2	19.2	23.2
		II	29.3	29.8	37.4	36.6	32.8	23.1	28.1
		III	20.1	19.8	25.7	25.2	22.5	15.9	19.3
	1/5	I	31.1	31.7	38.5	37.7	34.3	25.0	29.9
		II	37.8	39.0	46.5	45.6	41.7	30.2	36.3
		III	26.8	27.1	33.4	32.8	29.7	21.5	25.8
Cold Bay	1/10	I	46.8	48.7	55.9	54.9	51.0	38.2	45.2
		II	50.5	52.7	59.9	59.0	54.9	41.2	48.7
		III	43.1	44.6	51.8	50.9	47.1	35.1	41.5
	1/7	I	53.6	55.7	62.3	61.4	57.7	44.7	52.0
		II	57.5	60.0	66.4	65.5	61.8	48.1	55.8
		III	49.6	51.5	58.1	57.3	53.6	41.2	48.1
	1/5	I	61.9	64.2	69.8	68.8	65.7	53.2	60.4
		II	66.0	68.4	73.8	72.9	69.8	57.0	64.5
		III	57.9	59.9	65.8	64.8	61.7	49.5	56.4

Rural Alaska, fossil fuel is particularly expensive; wind power may contribute to holding costs affordable. The generation of wind power at Barrow would strongly be limited by the operating temperature range unless cold climate versions of wind turbines like Senvion's MM92 CCV with limits of −30˚C and lower would be deployed. At Annette and Juneau wind power is generally ineffective.

The typical distribution of the capacity factor is illustrated in **Figure 17**. Again, the General Electric 1.6 - 82.5 and Senvion MM92 have the highest and second highest capacity factor, respectively [15]. Nonetheless, capacity factors of more than 50% for $p=1/7$ and more than 60% for $p=1/5$ as obtained in Period I for most of these wind turbines in case of Cold Bay are extraordinary.

Figure 18 shows the relative decrease.

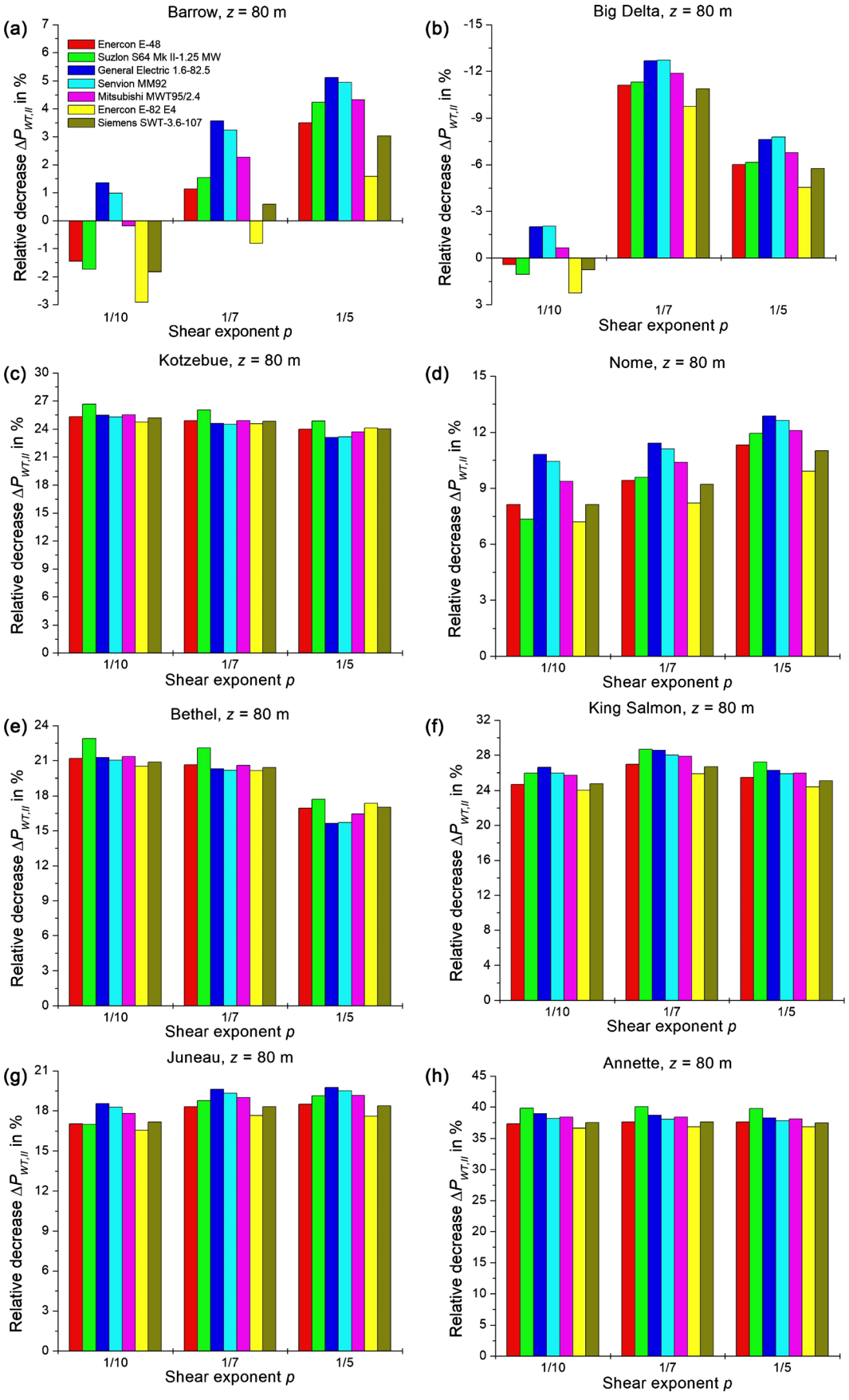
(a)
Barrow, z = 80 m
Enercon E-48
Suzlon S64 Mk II-1.25 MW
General Electric 1.6-82.5
Senvion MM92
Mitsubishi MWT95/2.4
Enercon E-82 E4
Siemens SWT-3.6-107
(b)
Big Delta, z = 80 m
(c)
Kotzebue, z = 80 m
(d)
Nome, z = 80 m
(e)
Bethel, z = 80 m
(f)
King Salmon, z = 80 m
(g)
Juneau, z = 80 m
(h)
Annette, z = 80 m
Relative decrease ΔP_WT,II in %
Shear exponent p
1/10
1/7
1/5

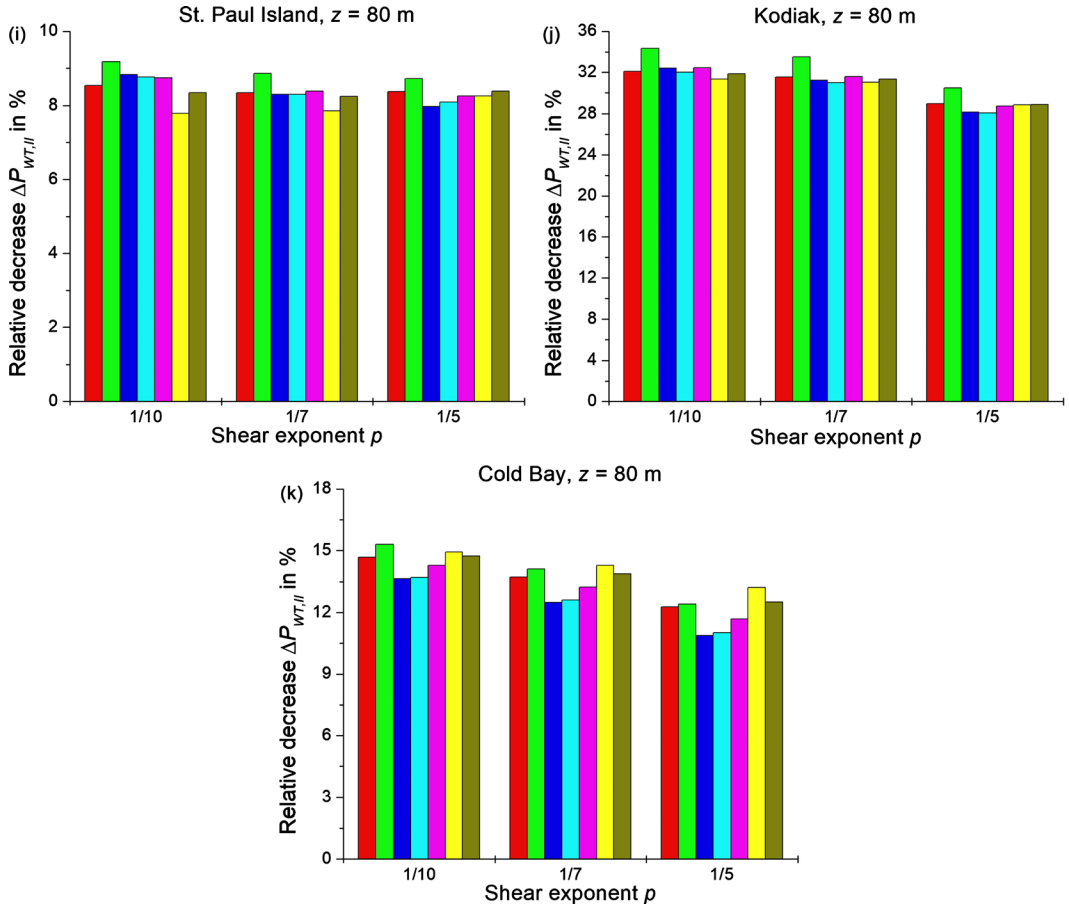

Figure 18. Relative decrease of predicted wind power at first-order weather stations (a) Barrow, (b) Big Delta, (c) Kotzebue, (d) Nome, (e) Bethel, (f) King Salmon, (g) Juneau, (h) Annette, (i) St. Paul Island, (j) Kodiak, and (k) Cold Bay for the seven wind turbines of different rated power (**Table 2**) as well as $p=1/10$, $p=1/7$, and $p=1/5$.

$$\Delta P_{WT,II}=\frac{\langle P_{WT,II}\rangle-\langle P_{WT,III}\rangle}{\langle P_{WT,II}\rangle}, \tag{5.2}$$

at each of the weather stations, where $\langle P_{WT,II}\rangle$ is the average wind power predicted for Period II and $\langle P_{WT,III}\rangle$ is that predicted for Period III. Besides Big Delta that suggests a relative increase in wind power of up to 12% for $p=1/7$, we found notable relative decreases in the predicted wind power of about 38% for Annette, followed by Kodiak (≈30%), King Salmon (≈26%), and Kotzebue (≈24%), where the effect of the shear exponents was marginal in these instances. Bethel with about 17% for $p=1/5$ and about 20% for $p=1/10$ and $p=1/7$, Juneau with about 18% hardly affected by the shear exponents, and Cold Bay with about 14% for $p=1/10$ to 10% for $p=1/5$ also show remarkable relative decreases in predicted wind power. In case of Nome, the relative decrease in the predicted wind power is less than 12%. However, the results notably depend on both the chosen wind turbine and the shear exponent. St. Paul Island exhibits a small relative decrease of about 8% hardly affected by the shear exponents. Barrow shows a relative increase mainly for $p=1/7$ and $p=1/5$, but this in-

crease is less than 5%.

In case of Annette, predicted wind power dramatically decreased due to the near-surface wind-speed stilling from Period II to Period III, but with respect to Period I, wind-power generation at Annette is generally ineffective. The same is true for Juneau despite the relative decrease in the predicted wind power is twice as small as compared with Annette. At Cold Bay, Bethel and Kotzebue, which were very good candidates for wind farms based on Period I, the near-surface wind-speed stilling notably shrinks wind-power generation. The same is true in the case of Kodiak and King Salmon.

For the purpose of simplification, the probabilities P_1, P_2, and P_3 given by Equations (4.5) to (4.7) were computed for Periods I, II, and III using a common cut-in wind speed of $v_{ci} = 3.0\ \mathrm{m \cdot s^{-1}}$ and a common wind speed of the rated power of $v_{pr} = 13.0\ \mathrm{m \cdot s^{-1}}$. The results are listed in **Table 9**.

6. Discussion and Conclusions

Based on wind-speed record of its 19 first-order weather stations, we analyze the near-surface wind-speed stilling in the State of Alaska, USA during the period reaching from January 1, 1984 to December 31, 2016 denoted as Period I. With exception of Big Delta that indicates an increase of 0.0157 $\mathrm{m \cdot s^{-1} \cdot a^{-1}}$, on average, all other first-order weather stations indicate declining trends in the near-surface wind speeds. In most cases, the average trends are less than −0.0300 $\mathrm{m \cdot s^{-1} \cdot a^{-1}}$, with exception of Gulkana that only exhibits a value of −0.0043 $\mathrm{m \cdot s^{-1} \cdot a^{-1}}$. The strongest trend was found at Homer with −0.0500 $\mathrm{m \cdot s^{-1} \cdot a^{-1}}$, on average, followed by Bettles with −0.0492 $\mathrm{m \cdot s^{-1} \cdot a^{-1}}$ and Yakutat with −0.0453 $\mathrm{m \cdot s^{-1} \cdot a^{-1}}$. At Barrow, however, the declining trend is marginal.

With respect to the National Renewable Energy Laboratory and the Alaska Energy Authority, the mean wind speed and the mean wind-power density computed for the Period I served to determine the wind-power class for each first-order weather station. This study finds Bettles, Fairbanks, McGrath, Gulkana, Talkeetna, Anchorage, Homer, and Yakutat are related to wind-power class 1, termed as "poor". These stations are impractical options for wind farms because they are unable to meet the basic criteria. The wind speeds at these locations would not be high enough to sufficiently supply power to the surrounding cities and communities, respectively. Also, they would experience a lot of days without receiving any power because the wind speed was not high enough to overcome the turbines cut-in wind speed. Thus, even though they indicate remarkable declining trends in the near-surface wind speeds, these first-order weather stations were not further considered in our prediction of wind power.

This wind-power potential, however, is of subordinate importance because wind turbines only extract a fraction of the kinetic energy from the wind field as characterized by the power efficiency. Since the wind turbine technology has notably improved during the past 35 years, we hypothetically used seven currently available wind turbines of different rated power (Enercon E-48, Suzlon

Table 9. Predicted probabilities P_1, P_2, and P_3 based on Equations (4.5) to (4.7) for first-order weather stations Barrow, Big Delta, Kotzebue, Nome, Bethel, King Salmon, Juneau, Annette, St. Paul Island, Kodiak, and Cold Bay and Periods I, II, and III using $p = 1/10$, $p = 1/7$ and $p = 1/5$.

Weather station	p	Period	P_1	P_2	P_3
Barrow WSO	1/10	I	0.098	0.879	0.023
		II	0.082	0.906	0.013
		III	0.120	0.851	0.029
	1/7	I	0.077	0.871	0.052
		II	0.061	0.904	0.035
		III	0.096	0.844	0.060
	1/5	I	0.056	0.825	0.118
		II	0.043	0.860	0.097
		III	0.072	0.804	0.124
Big Delta FAA/AMOS	1/10	I	0.393	0.568	0.040
		II	0.436	0.517	0.047
		III	0.377	0.590	0.033
	1/7	I	0.358	0.587	0.055
		II	0.413	0.528	0.059
		III	0.337	0.609	0.054
	1/5	I	0.342	0.574	0.084
		II	0.361	0.551	0.088
		III	0.300	0.623	0.077
Kotzebue WSO	1/10	I	0.186	0.773	0.041
		II	0.133	0.821	0.046
		III	0.243	0.720	0.037
	1/7	I	0.153	0.776	0.071
		II	0.108	0.810	0.082
		III	0.208	0.730	0.061
	1/5	I	0.121	0.751	0.127
		II	0.083	0.766	0.151
		III	0.170	0.723	0.107
Nome WSO	1/10	I	0.256	0.734	0.010
		II	0.208	0.787	0.005
		III	0.310	0.679	0.012
	1/7	I	0.215	0.763	0.022
		II	0.183	0.801	0.015
		III	0.267	0.710	0.023
	1/5	I	0.172	0.777	0.051

Continued

		II	0.141	0.818	0.041
		III	0.219	0.731	0.050
Bethel	1/10	I	0.119	0.871	0.011
		II	0.079	0.909	0.012
		III	0.146	0.843	0.011
	1/7	I	0.093	0.878	0.028
		II	0.061	0.905	0.034
		III	0.119	0.853	0.028
	1/5	I	0.069	0.855	0.076
		II	0.053	0.848	0.099
		III	0.088	0.842	0.070
King Salmon	1/10	I	0.209	0.790	0.001
		II	0.130	0.869	0.001
		III	0.264	0.733	0.002
	1/7	I	0.173	0.822	0.005
		II	0.090	0.907	0.003
		III	0.219	0.775	0.006
	1/5	I	0.135	0.848	0.017
		II	0.075	0.907	0.018
		III	0.180	0.801	0.019
Juneau	1/10	I	0.417	0.578	0.005
		II	0.366	0.630	0.004
		III	0.474	0.521	0.006
	1/7	I	0.376	0.614	0.010
		II	0.326	0.665	0.009
		III	0.433	0.557	0.010
	1/5	I	0.324	0.654	0.022
		II	0.269	0.711	0.020
		III	0.380	0.599	0.022
Annette WSO	1/10	I	0.365	0.633	0.002
		II	0.278	0.721	0.001
		III	0.458	0.540	0.001
	1/7	I	0.325	0.671	0.005
		II	0.238	0.758	0.004
		III	0.413	0.584	0.003
	1/5	I	0.268	0.719	0.013
		II	0.179	0.809	0.013

Continued

		III	0.355	0.636	0.009
St. Paul Island	1/10	I	0.062	0.839	0.099
		II	0.049	0.853	0.097
		III	0.079	0.823	0.098
	1/7	I	0.050	0.794	0.157
		II	0.040	0.801	0.159
		III	0.065	0.784	0.152
	1/5	I	0.037	0.712	0.251
		II	0.029	0.712	0.259
		III	0.049	0.713	0.238
Kodiak	1/10	I	0.195	0.793	0.012
		II	0.124	0.864	0.013
		III	0.251	0.739	0.009
	1/7	I	0.155	0.821	0.024
		II	0.102	0.868	0.030
		III	0.216	0.764	0.019
	1/5	I	0.131	0.812	0.056
		II	0.077	0.853	0.070
		III	0.173	0.782	0.045
Cold Bay	1/10	I	0.051	0.823	0.126
		II	0.037	0.824	0.140
		III	0.067	0.823	0.110
	1/7	I	0.041	0.768	0.191
		II	0.029	0.758	0.213
		III	0.055	0.778	0.167
	1/5	I	0.030	0.676	0.294
		II	0.021	0.652	0.327
		III	0.041	0.699	0.260

S64 Mark II-1.25 MW, General Electric 1.6 - 82.5, Senvion MM92, Mitsubishi MWT95/2.4, Enercon E-82 E4, and Siemens SWT-3.6-107) and three different shear exponents to assess the wind-power sustainability under changing wind regimes. These machines were chosen because of an increase in rated power by an increment of about 400 kW. The three shear exponents $p = 1/10$, $p = 1/7$, and $p = 1/5$ were considered to cover the range of wind power for various conditions of thermal stratification.

Based on the capacity factors for Period I, Cold Bay, St. Paul Island, Barrow, Kotzebue, and Bethel would be very good candidates for wind farms. Kodiak, Nome, King Salmon, and Big Delta may be considered for specific reasons like

the reduction of fossil fuel consumption which always plays a notable role in Rural Alaska. However, wind-power generation at Cold Bay, Bethel and Kotzebue is notably affected by this near-surface wind-speed stilling. The same is true in case of Kodiak and King Salmon, where the impact of this wind-speed stilling currently prevents sustainability of wind power at these two communities. As mentioned before, wind-power generation at Annette and Juneau is generally ineffective.

Cold Bay located in the Aleutians East Borough is an ideal site for a wind farm. It has a very high wind-power potential expressed by the wind-power class of 6, termed as "outstanding". As illustrated in **Figure 15**, the modes of the probability density functions range from 8.00 $\mathrm{m{\cdot}s^{-1}}$ for $p = 1/10$ to 9.67 $\mathrm{m{\cdot}s^{-1}}$ for $p = 1/5$. They broadly coincide with the maxima of the power efficiencies of machines like General Electric 1.6 - 82.5, Senvion MM92, and Mitsubishi MWT95/2.4. For all three periods, the probability P_1 is very low, but the P_3 is very high (see **Table 9**). The combination of these issues leads to extraordinarily high capacity factors. As illustrated in **Figure 19**, the average capacity factor ranges for Period I from 48.7% at $R_P = 0.133$ for $p = 1/10$ to 63.4% at $R_P = 0.303$ for $p = 1/5$, for Period II from 52.4% at $R_P = 0.145$ for $p = 1/10$ to 67.5% at $R_P = 0.334$ for $p = 1/5$, and for Period III from 44.9% at $R_P = 0.118$ for $p = 1/10$ to 59.4% at $R_P = 0.271$ for $p = 1/5$. Again, the results obtained for Periods II and III indicate a slight effect due to the near-surface wind-speed stilling (see **Figure 18**).

According to the Alaska Energy Data Gateway (https://akenergygateway.alaska.edu/community-data-summary/1418448/), between 2008 and 2013, the average power consumption (residential, commercial, and other) was about 2509 MWh. This means that one of the smaller wind turbines considered here would already be able to supply the community's power demand for much of the year without much support by Diesel generators. (Nevertheless, a spinning reserve is intended to protect the system against unforeseen events such as generation outages, sudden load changes or a combination of both.) The near-surface air temperature ranges from −25.0˚C observed on January 30, 2000 to 25.0˚C observed on July 13, 1960 [103]. Based on the period from 1971 to 2000, the lowest mean monthly minimum temperature is −5.0˚C (February) and the highest mean monthly temperature is 8.6˚C (August) [103]. Thus, the conditions of the common operating temperature range are usually fulfilled. Icing of the rotor blades, however, may occur during the cold season.

There is, however, a significant drawback. The Alaska-breeding population of Steller's Eider currently listed as threatened under the Endangered Species Act (ESA) and a State of Alaska species of special concern, regularly occurs on Izembek National Wildlife Refuge, near Cold Bay [104].

With respect to all three periods, the differences in wind-power generation between St. Paul Island located in the Bering Sea and Cold Bay are of secondary importance. St. Paul Island has a wind-power class of 6 as well. The probability

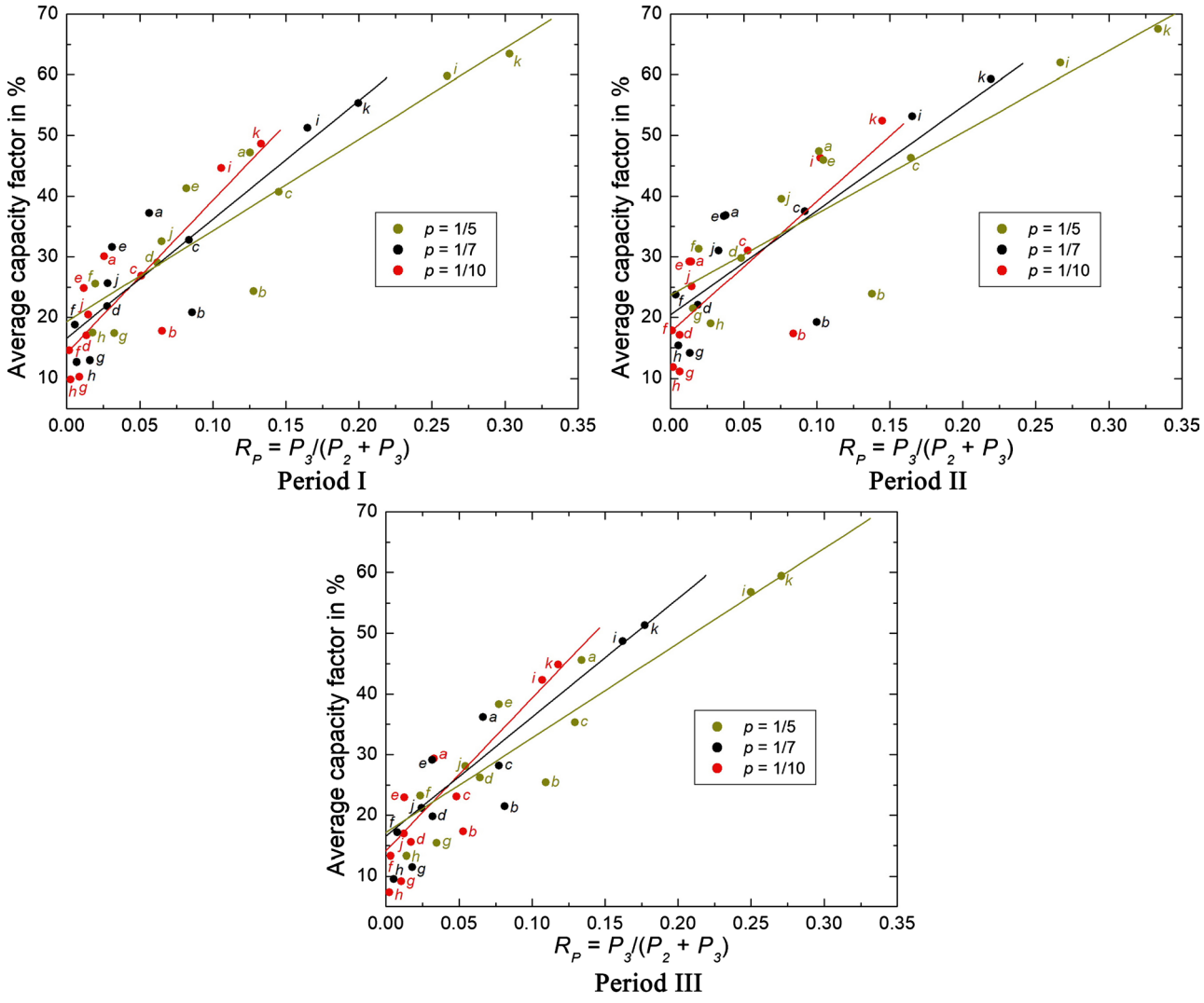

Figure 19. Capacity factor averaged over all wind turbines considered in this study versus the ratio $R_P = P_3/(P_2 + P_3)$ at first-order weather stations (a) Barrow, (b) Big Delta, (c) Kotzebue, (d) Nome, (e) Bethel, (f) King Salmon, (g) Juneau, (h) Annette, (i) St. Paul Island, (j) Kodiak, and (k) Cold Bay as well as $p = 1/10$, $p = 1/7$, and $p = 1/5$.

density functions determined for all three shear exponents and all three periods slightly differ from those of Cold Bay. Compared with those of Cold Bay, the modes are slightly shifted to lower wind speeds leading to a slightly higher probability P_1 and a slightly lower probability P_3. Thus, the capacity factors determined for St. Paul Island are somewhat lower than the corresponding ones of Cold Bay. As illustrated in Figure 19, the average capacity factor ranges for Period I from 44.6% at $R_P = 0.106$ for $p = 1/10$ to 59.8% at $R_P = 0.260$ for $p = 1/5$, for Period II from 46.3% at $R_P = 0.102$ for $p = 1/10$ to 62.0% at $R_P = 0.267$ for $p = 1/5$, and for Period III from 42.3% at $R_P = 0.107$ for $p = 1/10$ to 56.8% at $R_P = 0.250$ for $p = 1/5$. Again, the results obtained for the Periods II and III indicate a marginal effect due to the near-surface wind-speed stilling (see Figure 18).

Based on the Alaska Energy Data Gateway, the average power consumption

(residential, commercial and others) from 2009 to 2013 was about 3945 MWh mainly generated by using oil. The smaller wind turbines considered in this study would be able to supply the community's power demand for much of the year without much support by Diesel generators. The near-surface air temperature ranges from −28.3˚C observed on March 14, 1971 to 18.9˚C observed on August 25, 1987 [103]. Based on the period from 1971 to 2000, the lowest mean monthly minimum temperature is −7.3˚C (February) and the highest mean monthly temperature is 7.3˚C (August) [103]. Thus, the conditions of the common operating temperature range are usually fulfilled. Nevertheless, icing of the rotor blades may occur during the cold season.

St. Paul Island has a wind power history. As stated on its website (http://www.tdxpower.com/projects-commercial), the Tanadgusix Corporation (TDX) contracted with Northern Power designed and installed a wind/diesel system on St. Paul Island. The site is an airport and industrial complex with airline offices, equipment repair, and storage facilities. After completion, TDX Power began operating the first Native owned and operated independent, hybrid wind/diesel power plant in Alaska. Formally commissioned in 1999, this project capitalized on the emerging hybrid technology as a way to combat escalating fossil fuel prices. The major generation for the hybrid system is provided by a 225-kW Vestas V27 wind turbine. The system supplies electricity and space heat to an 88,000 SF industrial/airport facility and has reduced fuel consumption at the complex by 45%. Future plans involve expanding the wind power capacity and heating infrastructure. A total of 3 Vestas V27 wind turbines are currently installed, and a project is underway to connect the microgrid to the St. Paul municipal utility grid.

In its Systems Performance Analyses of Alaska Wind-Diesel Projects of 2009 (DOE/GO-102009-2712), the US Department of Energy (DOE) pointed out that in 2004 the wind turbine had a non-scheduled availability of 100% and a capacity factor of more than 40% and that the operating wind turbine has experienced a capacity factor of almost 32%. Using the power curve of the Vestas V27 machine taken from Mölders *et al.* [35] and assuming a hub height of $z = 37$ m we predicted the wind-power output for St. Paul Island for the purpose of comparison. Based on the daily mean wind speeds of Period III, we obtained for the shape parameters and the scale parameters, and the capacity factors following values: $k_W = 2.279$ and $c_W = 8.320\ \mathrm{m\cdot s^{-1}}$ for $p = 1/10$, $k_W = 2.271$ and $c_W = 8.794\ \mathrm{m\cdot s^{-1}}$ for $p = 1/7$, and $k_W = 2.284$ and $c_W = 9.497\ \mathrm{m\cdot s^{-1}}$ for $p = 1/5$, respectively. This means that the results of our analyses substantially agree with the results of this DOE report. In this case, the probability P_1 ranges from 10.3% for $p = 1/5$ to 13.8% for $p = 1/10$, P_2 ranges from 82.7% for $p = 1/5$ to 83.5% for $p = 1/10$, and P_3 ranges from 2.7% for $p = 1/10$ to 6.9% for $p = 1/5$, where the true value of $v_{ci} = 3.6\ \mathrm{m\cdot s^{-1}}$ and $v_{pr} = 14.6\ \mathrm{m\cdot s^{-1}}$ of the Vestas V27 wind turbine were considered. The modes of the probability functions are ranging from 6.33 $\mathrm{m\cdot s^{-1}}$ for $p = 1/10$ to 7.33 $\mathrm{m\cdot s^{-1}}$ for $p = 1/5$.

The capacity factor ranges from $C_{F,d} = 31.7\%$ at $R_P = 0.032$ for $p = 1/10$ to and $C_{F,d} = 40.7\%$ at $R_P = 0.077$ for $p = 1/5$.

Again, there is a significant drawback. St. Paul Island is home to millions of seabirds nesting in colonies along its steep shores. Rare birds are found here each year during spring migration. Also, St. Paul Island is considered a top North American bird watching destination [34].

Barrow located on the Chukchi Sea coast is the northernmost city of the United States. It has a remarkable wind-power potential expressed by the wind-power class of, at least, 3, termed as "fair". The probability density functions for all three shear exponents determined for all periods notably differ from those of Cold Bay. There is a shift in the modes by 2 $m \cdot s^{-1}$ or so to lower mean wind speeds. This leads to a remarkably higher probability P_1 and a notably lower probability P_3. Thus, the capacity factors determined for Barrow are notably lower than the corresponding ones of Cold Bay and St. Paul Island. As shown in **Figure 19**, the average capacity factor ranges for Period I from 30.1% at $R_P = 0.026$ for $p = 1/10$ to 47.2% at $R_P = 0.126$ for $p = 1/5$, for Period II from 29.2% at $R_P = 0.014$ for $p = 1/10$ to 47.4% at $R_P = 0.102$ for $p = 1/5$, and for Period III from 29.4% at $R_P = 0.033$ for $p = 1/10$ to 45.6% at $R_P = 0.134$ for $p = 1/5$. Since the decrease in the near-surface horizontal wind speed is marginal, the corresponding effect is negligible.

Based on the Alaska Energy Data Gateway, the average power consumption (residential and commercial) between 2008 and 2013 was about 48,909 MWh. The electricity was mainly produced using natural gas from nearby gas, only a very small amount was generated using oil. A power consumption of about 50 GWh would require numerous medium-scale wind turbines.

The generation of wind power at Barrow is strongly limited by the operating temperature range. The near-surface air temperature ranges from −48.9˚C observed on February 3, 1924 to 26.1˚C observed on July 13, 1993 [103]. Based on the period from 1971 to 2000, the lowest mean monthly minimum temperature is −30.0˚C (February) and the highest mean monthly temperature is 8.1˚C (July) [103]. Consequently, Barrow would require cold climate versions of wind turbines with limits of −30˚C and lower. Senvion's MM92 CCV nearly fulfils this requirement. Icing of the rotor blades, however, may occur during the cold season. Beside the low temperature range, Barrow's landscape has a great deal of lakes, ponds, and birds migrating. Wind turbines could impede the wildlife in the area by disrupting the migration and habitats of these animals. Based on these facts, we do not recommend the use of wind power at Barrow under the current conditions.

Kotzebue located at the north-western corner of the Baldwin Peninsula in the Kotzebue Sound, has a notable wind-power potential expressed by the wind-power class of 4, termed as "good". The wind-power density and average wind speed at hub height are relatively high signifying that it could generate a lot of power. The probability density functions determined for all three shear expo-

nents and all three periods, however, notably differ from those of Cold Bay. There is a notable shift in the modes to lower mean wind speeds ranging from 2 $m \cdot s^{-1}$ to 4 $m \cdot s^{-1}$ or so. Thus, P_1 is notably higher and P_3 is notably lower, and, hence, the capacity factors determined for Kotzebue are notably lower than the corresponding ones of Cold Bay and St. Paul Island. As illustrated in **Figure 19**, the average capacity factor ranges for Period I from 26.8% at $R_P = 0.051$ for $p = 1/10$ to 40.7% at $R_P = 0.145$ for $p = 1/5$, for Period II from 31.0% at $R_P = 0.053$ for $p = 1/10$ to 46.3% at $R_P = 0.164$ for $p = 1/5$, and for Period III from 23.1% at $R_P = 0.048$ for $p = 1/10$ to 35.3% at $R_P = 0.129$ for $p = 1/5$. The results obtained for the Periods II and III indicate a notable effect due to the near-surface wind-speed stilling (see **Figure 18**).

According to the Alaska Energy Data Gateway, the average power consumption (residential, commercial, and other) between 2009 and 2013 was about 20510 MWh. An average amount of 1955 MWh is related to wind power which corresponds to 9.5% (but 15.8% in 2013) of the net generation of electricity.

According to DOE's Systems Performance Analyses of Alaska Wind-Diesel Projects of 2009 (DOE/GO-102009-2711) the wind farm consists of fifteen 50-kW AOC 15/50 and Entegrity Wind Systems EW50; one 100-kW Northern Power Systems Northwind 100/19 A, and one remanufactured Vestas V17, *i.e.*, the total rated power is 0.925 MW. However, a power consumption of about 20 GWh would require some medium-scale wind turbines.

The near-surface air temperature ranges from −50.0˚C observed on March 16, 1930 to 29.4˚C observed on June 22, 1991 [103]. Based on the period from 1971 to 2000, the lowest mean monthly minimum temperature is −23.3˚C (February) and the highest mean monthly temperature is 15.6˚C (July). Thus, Kotzebue would require cold climate versions of wind turbines with limits of −30˚C. Icing of the rotor blades may occur during the cold season.

About 90 miles east of Kotzebue lies the Selawik National Wildlife Refuge. During the short Arctic summers, large numbers of white-fronted geese and tundra swans arrive along with sandhill cranes and a horde of other shorebirds.

Lastly, Bethel is the largest community on the Kuskokwim River, approximately 80 km upstream from where the river flows into Kuskokwim Bay. Bethel has a remarkable wind-power potential expressed by the wind-power class of, at least, 3 termed as "fair". The probability density functions for all three shear exponents determined for all periods notably differ from those of Cold Bay. There is a shift in the modes by more than 2 $m \cdot s^{-1}$ to lower mean wind speeds. Thus, P_1 is remarkably higher and P_3 is notably lower, and, hence, the capacity factors determined for Bethel are notably lower than the corresponding ones of Cold Bay and St. Paul Island. The average capacity factor ranges for Period I from 24.9% at $R_P = 0.012$ for $p = 1/10$ to 41.3% at $R_P = 0.082$ for $p = 1/5$, for Period II from 29.2% at $R_P = 0.013$ for $p = 1/10$ to 46.0% at $R_P = 0.105$ for $p = 1/5$, and for Period III from 23.0% at $R_P = 0.013$ for $p = 1/10$ to 38.3% at $R_P = 0.077$ for $p = 1/5$ (see **Figure 19**). As shown in

Figure 18, the results obtained for Periods II and III indicate a remarkable effect due to the near-surface wind-speed stilling.

According to the Alaska Energy Data Gateway, the average power consumption (residential, commercial, and other) between 2008 and 2013 was about 39749 MWh. A power consumption of about 40 GWh would require numerous medium-scale wind turbines.

The near-surface air temperature ranges from −44.4˚C observed on January 28, 1989 to 30.6˚C observed on August 9, 2003 [103]. Based on the period from 1971 to 2000, the lowest mean monthly minimum temperature is −17.4˚C (January) and the highest mean monthly temperature is 17.3˚C (July). Thus, the conditions of the common operating temperature range are usually fulfilled. Nevertheless, icing of the rotor blades may occur during the cold season.

A potential problem with Bethel is that it is surrounded by the Yukon Delta National Wildlife Refuge which supports one of the largest aggregations of water birds in the world. Thus, wind turbines could strongly impact the wildlife in that area by killing countless birds.

Based on our study, one may conclude that wind-stilling affects wind-power generation in Alaska to a notable degree. Thus, prior to installing new wind farms, assessments of suitability for power generation should look at the entire record of available data to identify trends in P_1, P_2, and P_3. Obviously, the distribution of these probabilities affects productivity. These aspects may also optimize the choice of turbine and sustainability of wind power. Also, like in the permitting process of power plants and other industrial complexes, a full environmental impact assessment must be performed to protect the subsistence lifestyle in the immediate area of the potential farm, wildlife, eco-systems and local climate. While the assessment of the impacts on endangered species, migrating birds and birds that are part of a subsistence lifestyle is straight forward, assessment of the impacts on local climate requires numerical modeling techniques. The mixing of air due to the rotor blades and the consequent more frequent neutral conditions alter the cloud and precipitation formation in the near-field. Such changes in the water cycle are known to affect ecosystems again with potential impacts on birds, fish and game and hence a subsistence lifestyle.

Acknowledgements

We would like to express our thanks to Prof. Dr. Gerd Wendler, Geophysical Institute of the University of Alaska Fairbanks, and Brian Hartmann for helpful comments and fruitful discussion.

Conflicts of Interest

The authors declare no conflicts of interest regarding the publication of this paper.

References

[1] McVicar, T.R., Roderick, M.L., Donohue, R.J., Li, L.T., Van Niel, T.G., Thomas, A.,

Grieser, J., Jhajharia, D., Himri, Y., Mahowald, N.M., Mescherskaya, A.V., Kruger, A.C., Rehman, S. and Dinpashoh, Y. (2012) Global Review and Synthesis of Trends in Observed Terrestrial Near-Surface Wind Speeds: Implications for Evaporation. *Journal of Hydrology*, **416-417**, 182-205. https://doi.org/10.1016/j.jhydrol.2011.10.024

[2] McVicar, T.R., Li, L., Van Niel, T.G., Li, L., Roderick, M.L., Rayner, D.P., Ricciardulli, L. and Donohue, R.J. (2008) Wind Speed Climatology and Trends for Australia, 1975-2006: Capturing the Stilling Phenomenon and Comparison with near-Surface Reanalysis Output. *Geophysical Research Letter*, **35**, L20403. https://doi.org/10.1029/2008GL035627

[3] Roderick, M.L., Rotstayn, L.D., Farquhar, G.D. and Hobbins, M.T. (2007) On the Attribution of Changing Pan Evaporation. *Geophysical Research Letters*, **34**, L17403. https://doi.org/10.1029/2007GL031166

[4] Klink, K. (1999) Trends in Mean Monthly Maximum and Minimum Surface Wind Speeds in the Coterminous United States, 1961 to 1990. *Climate Research*, **13**, 193-205. https://doi.org/10.3354/cr013193

[5] Pryor, S.C., Barthelmie, R.J., Young, D.T., Takle, E.S., Arritt, R.W., Flory, D.W., Gutowski, J.J., Nunes, A. and Road, J. (2009) Wind Speed Trends over the Contiguous United States. *Journal of Geophysical Research*, **114**, D14105. https://doi.org/10.1029/2008JD011416

[6] Tian, Q., Huang, G., Hu, K. and Niyogi, D. (2019) Observed and Global Climate Model Based Changes in Wind Power Potential over the Northern Hemisphere during 1979-2016. *Energy*, **167**, 1224-1235. https://doi.org/10.1016/j.energy.2018.11.027

[7] Xu, C., Gong, L., Jiang, T., Chen, D. and Singh, V.P. (2006) Analysis of Spatial Distribution and Temporal Trend of Reference Evapotranspiration and Pan Evaporation in Changjiang (Yangtze River) Catchment. *Journal of Hydrology*, **327**, 81-93. https://doi.org/10.1016/j.jhydrol.2005.11.029

[8] Xu, M., Chang, C.-P., Fu, C., Qi, Y., Robock, A., Robinson, D. and Zhang, H. (2006) Steady Decline of East Asian Monsoon Winds, 1969-2000: Evidence from Direct Ground Measurements of Wind Speed. *Journal Geophysical Research*, **111**, D24111. https://doi.org/10.1029/2006JD007337

[9] McVicar, T.R., Li, L., Van Niel, T.G., Hutchinson, M.F., Mu, X. and Liu, Z. (2005) Spatially Distributing 21 Years of Monthly Hydrometeorological Data in China: Spatio-Temporal Analysis of Fao-56 Crop Reference Evapotranspiration and Pan Evaporation in the Context of Climate Change. CSIRO Land and Water Technical Report 8/05.

[10] Pirazzoli, P.A. and Tomasin, A. (2003) Recent Near-Surface Wind Changes in the Central Mediterranean and Adriatic Areas. *International Journal of Climatology*, **23**, 963-973. https://doi.org/10.1002/joc.925

[11] Hundecha, Y., St-Hilaire, A., Ouarda, T.B.M.J., Adlouni, S.E. and Gachon, P. (2008) A Nonstationary Extreme Value Analysis for the Assessment of Changes Extreme Annual Wind Speed over the Gulf of St. Lawrence. *Journal of Applied Meteorology and Climatology*, **47**, 2745-2759. https://doi.org/10.1175/2008JAMC1665.1

[12] Tuller, S.E. (2004) Measured Wind Speed Trends on the West Coast of Canada. *International Journal of Climatology*, **24**, 1359-1374. https://doi.org/10.1002/joc.1073

[13] Azorin-Molina, C., Vicente-Serrano, S.M., McVicar, T.R., Jerez, S., Sanchez-Lorenzo, A., López-Moreno, J.-I., Revuelto, J., Trigo, R.M., Lopez-Bustins, J.A. and Espírito-Santo, F. (2014) Homogenization and Assessment of Observed near-Surface

Wind Speed Trends over Spain and Portugal, 1961-2011. *Journal of Climate*, **27**, 3692-3712. https://doi.org/10.1175/JCLI-D-13-00652.1

[14] Azorin-Molina, C., Guijarro, J.-A., McVicar, T.R., Vicente-Serrano, S.M., Chen, D., Jerez, S. and Espírito-Santo, F. (2016) Trends of Daily Peak Wind Gusts in Spain and Portugal, 1961-2014. *Journal of Geophysical Research*: *Atmospheres*, **121**, 1059-1078. https://doi.org/10.1002/2015JD024485

[15] Mölders, N., Khordakova, D., Dlugi, R. and Kramm, G. (2016) Sustainability of Wind Energy under Changing Wind Regimes—A Case Study. *Atmospheric and Climate Sciences*, **6**, 158-173. https://doi.org/10.4236/acs.2016.62014

[16] Hartmann, B. and Wendler, G. (2005) The Significance of the 1976 Pacific Climate Shift in the Climatology of Alaska. *Journal of Climate*, **18**, 4824-4839. https://doi.org/10.1175/JCLI3532.1

[17] Azorin-Molina, C., Menendez, M., McVicar, T.R., Acevedo, A., Vicente-Serrano, S.M., Cuevas, E., Minola, L. and Chen, D. (2017) Wind Speed Variability over the Canary Islands, 1948-2014: Focusing on Trend Differences at the Land-Ocean Interface and below-above the Trade-Wind Inversion Layer. *Climate Dynamics*, **50**, 4061-4081. https://doi.org/10.1007/s00382-017-3861-0

[18] Lynch, A.H., Curry, J.A., Brunner, R.D. and Maslanik, J.A. (2004) Toward an Integrated Assessment of the Impacts of Extreme Wind Events on Barrow, Alaska. *Bulletin of the American Meteorological Society*, **85**, 209-222. https://doi.org/10.1175/BAMS-85-2-209

[19] Kramm, G., Sellhorst, G., Ross, H.K., Cooney, J., Dlugi, R. and Mölders, N. (2016) On the Maximum of Wind Power Efficiency. *Journal of Power and Energy Engineering*, **4**, 1-39. https://doi.org/10.4236/jpee.2016.41001

[20] Hesselberg, T. (1926) Die Gesetze Der Ausgeglichenen Atmosphärischen Bewegungen. *Beiträge zur Physik der freien Atmosphäre*, **12**, 141-160.

[21] van Mieghem, J. (1973) Atmospheric Energetics. Clarendon Press, Oxford.

[22] Cox, G. (1995) Basic Considerations. In: Cox, G., Ed., *Combustion Fundamentals of Fire*, Academic Press, London, New York, 3-30.

[23] Kramm, G., Dlugi, R. and Lenschow, D.H. (1995) A Re-Evaluation of the Webb Correction Using Density-Weighted Averages. *Journal of Hydrology*, **166**, 283-292. https://doi.org/10.1016/0022-1694(94)05088-F

[24] Kramm, G. and Meixner, F.X. (2000) On the Dispersion of Trace Species in the Atmospheric Boundary Layer: A Re-Formulation of the Governing Equations for the Turbulent Flow of the Compressible Atmosphere. *Tellus A*: *Dynamic Meteorology and Oceanography*, **52**, 500-522. https://doi.org/10.3402/tellusa.v52i5.12279

[25] Kramm, G., Amaja, D.J., Foken, T. and Mölders, N. (2013) Hans A. Panofsky's Integral Similarity Function-at Fifty. *Atmospheric and Climate Sciences*, **3**, 581-594. https://doi.org/10.4236/acs.2013.34061

[26] Herbert, F. (1975) Irreversible Prozesse Der Atmosphäre—3. Teil (Phänomenologische Theorie Mikroturbulenter Systeme). *Beiträge zur Physik der Atmosphäre*, **48**, 1-29.

[27] Pichler, H. (1984) Dynamik Der Atmosphäre. Bibliographisches Institut, Berlin.

[28] Montgomery, R.B. (1954) Convection of Heat. *Archiv für Meteorologie*, *Geophysik und Bioklimatologie*, *Serie A*, **7**, 125-132. https://doi.org/10.1007/BF02277911

[29] Fortak, H. (1969) Zur Energetik Der Planetarischen Grenzschicht. *Annalen der Meteorologie* (*NF*), **4**, 157-162.

[30] Libby, P.A. and Williams, F.A. (1980) Turbulent Reacting Flows. Springer-Verlag, Berlin. https://doi.org/10.1007/3-540-10192-6

[31] Thomson, D. (1995) The Parameterization of the Vertical Dispersion of a Scalar in the Atmospheric Boundary Layer: by Venkatram A. (1993) *Atmospheric Environment* **27A**, 1963-1966. *Atmospheric Environment*, **29**, 1343. https://doi.org/10.1016/1352-2310(94)00326-G

[32] Venkatram, A. (1998) Response. *Atmospheric Environment*, **32**, 259. https://doi.org/10.1016/S1352-2310(96)00078-7

[33] Kowalski, A.S. (2012) Exact Averaging of Atmospheric State and Flow Variables. *Journal of the Atmospheric Sciences*, **69**, 1750-1757. https://doi.org/10.1175/JAS-D-11-0299.1

[34] Ross, H.K., Cooney, J., Hinzman, M., Smock, S., Sellhorst, G., Dlugi, R., Mölders, N. and Kramm, G. (2014) Wind Power Potential in Interior Alaska from a Micrometeorological Perspective. *Atmospheric and Climate Sciences*, **4**, 100-121. https://doi.org/10.4236/acs.2014.41013

[35] Mölders, N., Khordakova, D., Gende, S. and Kramm, G. (2015) Uncertainty of Wind Power Usage in Complex Terrain—A Case Study. *Atmospheric and Climate Sciences*, **5**, 228-244. https://doi.org/10.4236/acs.2015.53017

[36] Menne, M.J., Durre, I., Vose, R.S., Gleason, B.E. and Houston, T.G. (2012) An Overview of the Global Historical Climatology Network-Daily Database. *Journal of Atmospheric and Oceanic Technology*, **29**, 897-910. https://doi.org/10.1175/JTECH-D-11-00103.1

[37] Mölders, N., Tran, H.N.Q., Cahill, C.F., Leelasakultum, K. and Tran, T.T. (2012) Assessment of Wrf/Chem $PM_{2.5}$ Forecasts Using Mobile and Fixed Location Data from the Fairbanks, Alaska Winter 2008/09 Field Campaign. *Atmospheric Pollution Research*, **3**, 180-191. https://doi.org/10.5094/APR.2012.018

[38] Haltiner, G.J. and Martin, F.L. (1957) Dynamical and Physical Meteorology. McGraw-Hill Book Company, New York.

[39] Pal Arya, S. (1988) Introduction to Micrometeorology. Academic Press, San Diego, CA.

[40] Schwartz, M. and Elliot, D. (2006) Wind Shear Characteristics at Central Plains Tall Towers. In: *Windpower* 2006 *Conference*, Pittsburg, PA.

[41] Storm, B.A. (2008) Modeling of Low-Level Jets over the Great Plains: Implications for Wind Energy. In: *Wind Science and Engineering Research Center*, Texas Tech University, Lubbock, TX.

[42] Storm, B., Dudhia, J., Basu, S., Swift, A. and Giammanco, I. (2009) Evaluation of the Weather Research and Forecasting Model on Forecasting Low-Level Jets: Implications for Wind Energy. *Wind Energy*, **12**, 81-90. https://doi.org/10.1002/we.288

[43] Frost, R. (1947) The Velocity Profile in the Lowest 400 Feet. *Meteorological Magazine*, **76**, 14-17.

[44] Sisterson, D.L. and Frenzen, P. (1978) Nocturnal Boundary-Layer Wind Maxima and the Problem of Wind Power Assessment. *Environmental Science & Technology*, **12**, 218-221. https://doi.org/10.1021/es60138a014

[45] Irwin, J.S. (1979) A Theoretical Variation of the Wind Profile Power-Law Exponent as a Function of Surface Roughness and Stability. *Atmospheric Environment*, **13**, 191-194. https://doi.org/10.1016/0004-6981(79)90260-9

[46] Sisterson, D.L., Hicks, B.B., Coulter, R.L. and Wesely, M.L. (1983) Difficulties in Using Power Laws for Wind Energy Assessment. *Solar Energy*, **31**, 201-204. https://doi.org/10.1016/0038-092X(83)90082-8

[47] Giebel, G. and Gryning, S.E. (2004) Shear and Stability in High Met Masts, and

How WAsP Treats It. The Science of Making Torque from Wind. In: *Technical Report*, European Wind Energy Association, Delft, The Netherlands.

[48] Zhang, X., Yang, C. and Li, S. (2019) Influence of the Heights of Low-Level Jets on Power and Aerodynamic Loads of a Horizontal Axis Wind Turbine Rotor. *Atmosphere*, **10**, 1-16.

[49] Deardorff, J.W. (1978) Efficient Prediction of Ground Surface Temperature and Moisture, with Inclusion of a Layer of Vegetation. *Journal of Geophysical Research: Oceans*, **83**, 1889-1903. https://doi.org/10.1029/JC083iC04p01889

[50] McCumber, M.C. (1980) A Numerical Simulation of the Influence of Heat and Moisture Fluxes Upon Mesoscale Circulation. University of Virginia, Charlottesville, VA.

[51] Pielke, R.A. (1984) Mesoscale Meteorological Modeling. Academic Press, Orlando, FL.

[52] Meyers, T. and Paw U, K.T. (1986) Testing of a Higher-Order Closure Model for Modeling Airflow within and above Plant Canopies. *Boundary-Layer Meteorology*, **37**, 297-311. https://doi.org/10.1007/BF00122991

[53] Meyers, T. and Paw U, K.T. (1987) Modelling the Plant Canopy Micrometeorology with Higher-Order Closure Principles. *Agricultural and Forest Meteorology*, **41**, 143-163. https://doi.org/10.1016/0168-1923(87)90075-X

[54] Sellers, P.J., Mintz, Y., Sud, Y.C. and Dalcher, A. (1986) A Simple Biosphere Model (Sib) for Use within General-Circulation Models. *Journal of the Atmospheric Sciences*, **43**, 505-531. https://doi.org/10.1175/1520-0469(1986)043<0505:ASBMFU>2.0.CO;2

[55] Braud, I., Dantasantonino, A.C., Vauclin, M., Thony, J.L. and Ruelle, P. (1995) A Simple Soil-Plant-Atmosphere Transfer Model (SiSPAT) Development and Field Verification. *Journal of Hydrology*, **166**, 213-250. https://doi.org/10.1016/0022-1694(94)05085-C

[56] Kramm, G., Beier, N., Foken, T., Muller, H., Schröder, P. and Seiler, W. (1996) A Svat Scheme for NO, NO_2, and O_3—Model Description and Test Results. *Meteorology and Atmospheric Physics*, **61**, 89-106. https://doi.org/10.1007/BF01029714

[57] Kramm, G., Dlugi, R., Müller, H. and Paw, U.K.T. (1998) Numerische Untersuchungen Zum Austausch Von Impuls, Sensibler Wärme Und Masse Zwischen Atmosphäre Und Hoher Vegetation. *Annalen der Meteorologie*, **37**, 475-476.

[58] Ziemann, A. (1998) Numerical Simulation of Meteorological Quantities in and above Forest Canopies. *Meteorologische Zeitschrift*, **7**, 120-128.

[59] Su, H.B., Shaw, R.H. and Paw U, K.T. (2000) Two-Point Correlation Analysis of Neutrally Stratified Flow within and above a Forest from Large-Eddy Simulation. *Boundary-Layer Meteorology*, **94**, 423-460. https://doi.org/10.1023/A:1002430213742

[60] Pyles, R.D., Weare, B.C. and Paw U, K.T. (2000) The UCD Advanced Canopy-Atmosphere-Soil Algorithm: Comparisons with Observations from Different Climate and Vegetation Regimes. *Quarterly Journal of the Royal Meteorological Society*, **126**, 2951-2980. https://doi.org/10.1002/qj.49712656917

[61] Pyles, R.D., Weare, B.C., Paw U, K.T. and Gustafson, W. (2003) Coupling between the University of California, Davis, Advanced Canopy-Atmosphere-Soil Algorithm (ACASA) and Mm5: Preliminary Results for July 1998 for Western North America. *Journal of Applied Meteorology*, **42**, 557-569. https://doi.org/10.1175/1520-0450(2003)042<0557:CBTUOC>2.0.CO;2

[62] Mölders, N., Haferkorn, U., Döring, J. and Kramm, G. (2003) Long-Term Investigations on the Water Budget Quantities Predicted by the Hydro-Thermodynamic Soil Vegetation Scheme (HTSVS)—Part I: Description of the Model and Impact of Long-Wave Radiation, Roots, Snow, and Soil Frost. *Meteorology and Atmospheric Physics*, **84**, 115-135. https://doi.org/10.1007/s00703-002-0578-2

[63] Mölders, N., Haferkorn, U., Döring, J. and Kramm, G. (2003) Long-Term Investigations on the Water Budget Quantities Predicted by the Hydro-Thermodynamic Soil Vegetation Scheme (HTSVS)—Part II: Evaluation, Sensitivity, and Uncertainty. *Meteorology and Atmospheric Physics*, **84**, 137-156. https://doi.org/10.1007/s00703-002-0596-0

[64] Kramm, G. and Dlugi, R. (2011) Scrutinizing the Atmospheric Greenhouse Effect and Its Climatic Impact. *Natural Science*, **3**, 971-998. https://doi.org/10.4236/ns.2011.312124

[65] Panofsky, H.A. (1963) Determination of Stress from Wind and Temperature Measurements. *Quarterly Journal of the Royal Meteorological Society*, **89**, 85-94. https://doi.org/10.1002/qj.49708937906

[66] Paulson, C.A. (1970) The Mathematical Representation of Wind Speed and Temperature Profiles in the Unstable Atmospheric Surface Layer. *Journal of Applied Meteorology*, **9**, 857-861. https://doi.org/10.1175/1520-0450(1970)009<0857:TMROWS>2.0.CO;2

[67] Kramm, G. and Herbert, F. (2009) Similarity Hypotheses for the Atmospheric Surface Layer Expressed by Non-Dimensional Characteristic Invariants: A Review. *The Open Atmospheric Science Journal*, **3**, 48-79. https://doi.org/10.2174/1874282300903010048

[68] Kramm, G. and Mölders, N. (2005) On the Transfer of Momentum, Sensible Heat and Matter across the Interfacial Sublayer over Aerodynamically Smooth Surfaces. *Bulletin of the Calcutta Mathematical Society*, **2**, 105-120.

[69] Pohlhausen, E. (1921) Der Wärmeaustausch Zwischen Festen Körpern Und Flüssigkeiten Mit Kleiner Reibung Und Kleiner Wärmeleitung. *ZAMM: Journal of Applied Mathematics and Mechanics/Zeitschrift für Angewandte Mathematik und Mechanik*, **1**, 115-121. https://doi.org/10.1002/zamm.19210010205

[70] Dipprey, D.F. and Sabersky, R.H. (1963) Heat and Momentum Transfer in Smooth and Rough Tubes at Various Prandtl Numbers. *International Journal of Heat and Mass Transfer*, **6**, 329-353. https://doi.org/10.1016/0017-9310(63)90097-8

[71] Owen, P.R. and Thomson, W.R. (1963) Heat Transfer across Rough Surfaces. *Journal of Fluid Mechanics*, **15**, 321-334. https://doi.org/10.1017/S0022112063000288

[72] Chamberlain, A.C. (1968) Transport of Gases to and from Surfaces with Bluff and Wave-Like Roughness Elements. *Quarterly Journal of the Royal Meteorological Society*, **94**, 318-332. https://doi.org/10.1002/qj.49709440108

[73] Yaglom, A.M. and Kader, B.A. (1974) Heat and Mass Transfer between a Rough Wall and Turbulent Fluid Flow at High Reynolds and Péclet Numbers. *Journal of Fluid Mechanics*, **62**, 601-622.

[74] Brutsaert, W. (1975) The Roughness Length for Water Vapor, Sensible Heat, and Other Scalars. *Journal of the Atmospheric Sciences*, **32**, 2028-2031. https://doi.org/10.1175/1520-0469(1975)032<2029:TRLFWV>2.0.CO;2

[75] Brutsaert, H.W. (1982) Exchange Processes at the Earth-Atmosphere Interface. In: Plate, E., Ed., *Engineering Meteorology*, Elsevier, New York, 319-369.

[76] Kramm, G., Dlugi, R., and Mölders, N. (2002) Stanton Numbers of Heat and Matter for Aerodynamically Smooth Surfaces: Basic Considerations and Evaluation. *Mete-*

orology and Atmospheric Physics, **79**, 173-194. https://doi.org/10.1007/s007030200002

[77] Monin, A.S. and Obukhov, A.M. (1954) Osnovnye Zakonomernosti Turbulentnogo Peremešivanija V Prizemnom Sloe Atmosfery. *Trudy Geofiz Inst AN SSSR*, **24**, 163-187.

[78] Smock, S. and Kramm, G. (2011), Power-Law and Logarithmic Wind Profiles: A Synthesis. In: *NSF REU Site Program in Atmospheric Sciences*, University of Alaska Fairbanks, Geophysical Institute, Fairbanks, AK.

[79] Tangermann-Dlugi, G. (1982) Numerische Simulationen Atmosphärischer Grenzschichtströmungen Über Langgestreckten Mesoskaligen Hügelketten Bei Neutraler Thermischer Schichtung. In: *Wissenschaftliche Berichte des Instituts für Meteorologie und Klimaforschung des Karlsruher Instituts für Technologie*, Karlsruher Institut für Technologie, Karlsruhe, Germany.

[80] Dorwarth, G. (1986) Numerische Berechnung Des Druckwiderstandes Typischer Geländeformen. In: *Wissenschaftliche Berichte des Instituts für Meteorologie und Klimaforschung des Karlsruher Instituts für Technologie*, Karlsruhe Institut für Technologie, Karlsruhe.

[81] Adrian, G. and Fiedler, F. (1991) Simulation of Unstationary Wind and Temperature Fields over Complex Terrain and Comparison with Observations. *Contribution to Atmospheric Physics*, **64**, 27-48.

[82] Pielke, R.A., Cotton, W.R., Walko, R.L., Tremback, C.J., Lyons, W.A., Grasso, L.D., Nicholls, M.E., Moran, M.D., Wesley, D.A., Lee, T.J. and Copeland, J.H. (1992) A Comprehensive Meteorological Modeling System—RAMS. *Meteorology and Atmospheric Physics*, **49**, 69-91. https://doi.org/10.1007/BF01025401

[83] Kapitza, H. and Eppel, D.P. (1992) The Non-Hydrostatic Mesoscale Model Gesima, Part I: Dynamical Equations and Tests. *Contribution to Atmospheric Physics*, **65**, 129-146.

[84] Eppel, D.P., Kapitza, H., Claussen, M.J., D., Koch, W., Levkov, L., Mengelkamp, H.-T. and Werrmann, N. (1995) The Nonhydrostatic Mesoscale Model Gesima, Part II: Parameterizations and Applications. *Contribution to Atmospheric Physics*, **68**, 15-41.

[85] Mölders, N. and Raabe, A. (1997) Testing the Effect of a Two-Way-Coupling of a Meteorological and a Hydrologic Model on the Predicted Local Weather. *Atmospheric Research*, **45**, 81-107. https://doi.org/10.1016/S0169-8095(97)00035-5

[86] Baidya Roy, S. and Traiteur, J.J. (2010) Impacts of Wind Farms on Surface Air Temperatures. *Proceedings of the National Academy of Sciences of the United States of America*, **107**, 17899-17904. https://doi.org/10.1073/pnas.1000493107

[87] Miller, L.M., Brunsell, N.A., Mechem, D.B., Gans, F., Monaghan, A.J., Vautard, R., Keith, D.W. and Kleidon, A. (2015) Two Methods for Estimating Limits to Large-Scale Wind Power Generation. *Proceedings of the National Academy of Sciences of the United States of America*, **112**, 11169-11174. https://doi.org/10.1073/pnas.1408251112

[88] Fitch, A.C. (2015) Climate Impacts of Large-Scale Wind Farms as Parameterized in a Global Climate Model. *Journal of Climate*, **28**, 6160-6180. https://doi.org/10.1175/JCLI-D-14-00245.1

[89] Barthelmie, R.J., Frandsen, S.T., Nielsen, M.N., Pryor, S.C., Rethore, P.-E. and Jørgensen, H.E. (2007) Modelling and Measurements of Power Losses and Turbulence Intensity in Wind Turbine Wakes at Middelgrunden Offshore Wind Farm. *Wind Energy*, **10**, 517-528. https://doi.org/10.1002/we.238

[90] Barthelmie, R.J. and Jensen, L.E. (2010) Evaluation of Wind Farm Efficiency and Wind Turbine Wakes at the Nysted Offshore Wind Farm. *Wind Energy*, **13**, 573-586. https://doi.org/10.1002/we.408

[91] Barthelmie, R.J., Pryor, S.C., Frandsen, S.T., Hansen, K.S., Schepers, J.G., Rados, K., Schlez, W., Neubert, A., Jensen, L.E. and Neckelmann, S. (2010) Quantifying the Impact of Wind Turbine Wakes on Power Output at Offshore Wind Farms. *Journal of Atmospheric and Oceanic Technology*, **27**, 1302-1317. https://doi.org/10.1175/2010JTECHA1398.1

[92] Schepers, J.G., Obdam, T.S. and Prospathopoulos, J. (2012) Analysis of Wake Measurements from the Ecn Wind Turbine Test Site Wieringermeer, EWTW. *Wind Energy*, **15**, 575-591. https://doi.org/10.1002/we.488

[93] Hirth, B.D. and Schroeder, J.L. (2013) Documenting Wind Speed and Power Deficits Behind a Utility-Scale Wind Turbine. *Journal of Applied Meteorology and Climatology*, **52**, 39-46. https://doi.org/10.1175/JAMC-D-12-0145.1

[94] Rooijmans, P. (2004) Impact of a Large-Scale Offshore Wind Farm on Meteorology: Numerical Simulations with a Mesoscale Circulation Mod. Utrecht University, Utrecht, The Netherlands.

[95] Rankine, W.J.M. (1865) On the Mechanical Principles of the Action of Propellers. *Transaction of the Institute of Naval Architects*, **6**, 13-39.

[96] Froude, W. (1878) On the Elementary Relation between Pitch, Slip and Propulsive Efficiency. *Transaction of the Institute of Naval Architects*, **19**, 22-33.

[97] Froude, R.E. (1889) On the Part Played in Propulsion by Difference in Pressure. *Transaction of the Institute of Naval Architects*, **30**, 390-405.

[98] Betz, A. (1920) Das Maximum Der Theoretisch Möglichen Ausnützung Des Windes Durch Windmotoren. *Zeitschrift für das gesamte Turbinenwesen*, **26**, 307-309.

[99] Joukowsky, N.E. (1920) Windmill of the NEJ Type. Transactions of the Central Institute for Aero-Hydrodynamics of Moscow. (In Russian)

[100] Weibull, W. (1951) A Statistical Distribution Function of Wide Applicability. *ASME Journal of Applied Mechanics*, **18**, 293-297.

[101] Justus, C.G., Hargraves, W.R. and Yalcin, A. (1976) Nationwide Assessment of Potential Output from Wind-Powered Generators. *Journal of Applied Meteorology*, **15**, 673-678. https://doi.org/10.1175/1520-0450(1976)015<0673:NAOPOF>2.0.CO;2

[102] Cooney, J. and Kramm, G. (2012) Determining Viable Locations for Wind Farms in Alaska. In: *NSF REU Site Program in Atmospheric Sciences*, University of Alaska Fairbanks, Geophysical Institute, Fairbanks, AK.

[103] Shulski, M. and Wendler, G. (2007) The Climate of Alaska. University of Alaska Press, Fairbanks, AK.

[104] Baker, A. and Bolling, L. (2010) Renewable Energy Resource Assessment for the Communities of Cold Bay, False Pass, and Nelson Lagoon. Alaska Energy Authority, Anchorage, AK.